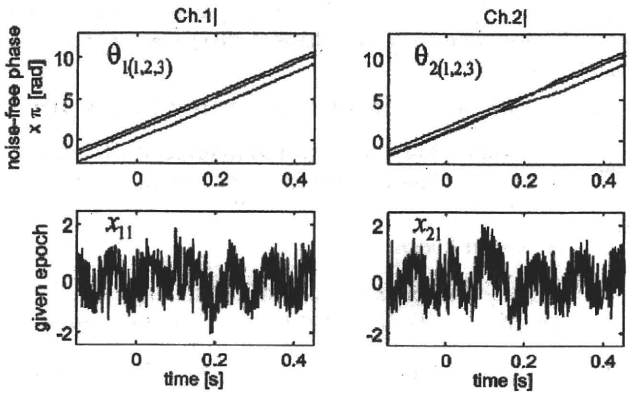

Fig. 2. Settings of Simulation I. (left column) xEG time series of channel 1. (right column) xEG time series of channel 2. (top row) Stacked given phases without noise for the first three epochs. (bottom row) Given xEG time series for the first epoch.

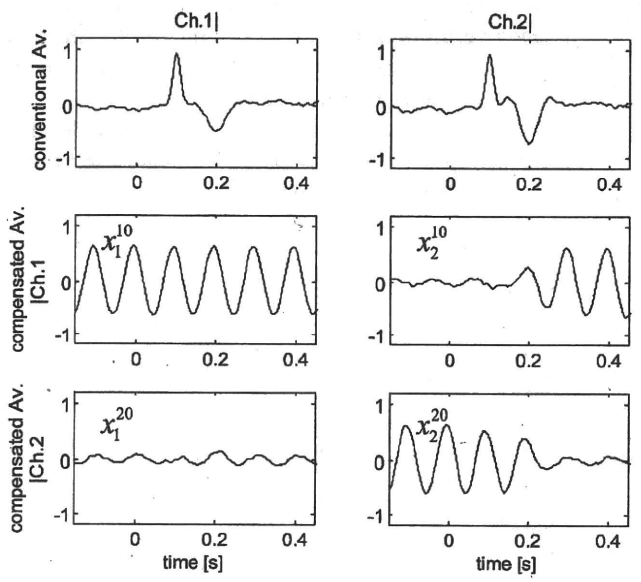

Fig. 3. Results of Simulation I. (left column) xEG time series of channel 1. (right column) xEG time series of channel 2. (top row) Conventional averages. (middle row) averages compensated by instantaneous phases of channel 1. (bottom row) Averages compensated by instantaneous phases of channel 2.

B. Conventional Averages

The top row of Fig. 3 shows the conventional averages of channels 1 and 2. The given ongoing alpha-band activities are almost canceled out in both channels. The stimulus-evoked activities of channels 1 and 2 were extracted without and with distortion, respectively. The difference between channels is due to the directional phase modulation from channel 1 to channel 2. In the meantime of the phase modulation, the instantaneous phases of the given epochs were not uniformly distributed from 0 to 2π. Therefore, the conventional average included stimulus-induced activities via the phase modulation.

C. Phase-Compensated Averages

Phase-compensated averaging was performed under the following conditions. The passband for narrow-bandpass filtering and the duration G [both in Fig. 1(a)] were 8–26 Hz (from alpha- to beta-band) and -0.05 to 0.05 s. The instantaneous phases were calculated at $n_0 = 0$ s. The passband for wide-bandpass filtering was 1–52 Hz [see Fig. 1(b)]. Both narrow- and wide-bandpass filtering were performed as part of the DHT by padding additional zeros to the stopbands.

The bottom two rows show the phase-compensated averages in 2×2 matrix form; i.e., the columns indicate channels for averaging [m in phase-compensated average (2)], and the rows indicate channels for the instantaneous phase calculation [l in phase-compensated average (2)]. Thus, the "diagonal" and "off-diagonal" panels indicate auto and cross averages, respectively. Note that only the real parts are presented because phase-compensation (1) rotates the narrow-band part of the complex xEG epochs onto the real axis. Although the auto average $\bar{x}_1^{10}[n]$ showed stable alpha-band activity all the time, the auto average $\bar{x}_2^{20}[n]$ decayed after 0.2 s. On the other hand, although the cross average $\bar{x}_1^{20}[n]$ showed small activity all the time, the cross average $\bar{x}_2^{10}[n]$ increased in amplitude after 0.1 s. The reason these phenomena occurred was that channel 2 was modulated by channel 1 for 0.1–0.2 s but channel 1 was not influenced by channel 2 all the time under phase setting (7). Therefore, phase-compensated averaging revealed not only the relationship between channels 1 and 2 but also their directional relationship, namely from channel 1 to channel 2.

To avoid having the stimulus-evoked activity leak into the phase-compensated averages, the duration G should be one in which the instantaneous phases over epochs are almost uniformly distributed. In such a selection, the average of the stimulus-evoked activity complex-weighted with uniformly distributed phases will theoretically be zero, since the stimulus-evoked activity is common to all epochs. Accordingly, the ongoing spontaneous activities can be selectively averaged in the phase-locking sense by using the parameters of the instantaneous phase calculation.

IV. Simulation II: Stimulus-Induced Activities via Changes of Ongoing Spontaneous Activities

Two simulations were performed to analyze stimulus-induced activities via changes of ongoing spontaneous activities. The additive stimulus-evoked activity and random numbers used in Simulation I were not given. Since the given xEG epochs of both simulations in Simulation II were noise-free and narrow-band, narrow- and wide-bandpass filtering were not performed. The sampling frequency was 1 kHz and the duration G for determining the instantaneous phases was -0.35 to -0.25 s (namely, $n_0 = -0.3$ s).

A. Phase-Reset

Unlike the random phase modulation in Simulation I, a systematic phase modulation to simulate a phase-reset was prepared. First, single-channel and 200-trial ($q = 0, 1, \ldots, 199$)

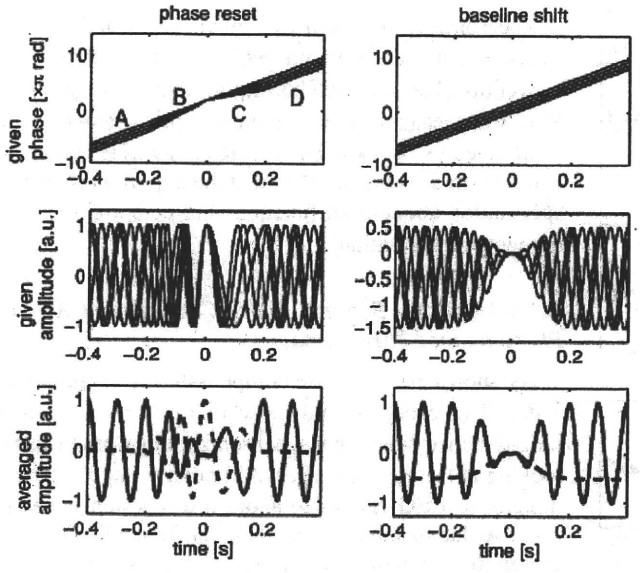

Fig. 4. Simulation II for xEG generation models. (left column) Phase reset model. (right column) Baseline shift model. (top row) Stacked given phases ($q = 0, 60, 120, 180$). (middle row) Stacked given xEG time series ($q = 0, 60, 120, 180$). (bottom row) Results of Simulation II. The dashed and solid lines indicate conventional averaging and phase-compensated averaging results, respectively.

phases are given as

$$\theta_q^{\mathrm{PR}}(t) = \begin{cases} \psi_q^{\mathrm{PR}}(t), & t \le -0.2,\ 0.2 < t \\ (\psi_{199}^{\mathrm{PR}}(0) - \psi_q^{\mathrm{PR}}(-0.2))t/0.2 + \psi_{199}^{\mathrm{PR}}(0), & -0.2 < t \le 0 \\ (\psi_{199}^{\mathrm{PR}}(0.2) - \psi_q^{\mathrm{PR}}(0))t/0.2 + \psi_{199}^{\mathrm{PR}}(0), & 0 < t \le 0.2 \end{cases} \tag{10}$$

where

$$\psi_q^{\mathrm{PR}}(t) = 2\pi 10t + \frac{2\pi q}{200}. \tag{11}$$

Here PR stands for phase reset. The top-left panel in Fig. 4 illustrates four samples of the given phase (10). The phases that were uniformly distributed in duration A (−0.4 to −0.2 s) linearly changed to a point distribution in duration B (−0.2 to 0 s), and *vice versa* in durations C (0–0.2 s) and D (0.2–0.4 s). The xEG epochs are given as

$$x_q^{\mathrm{PR}}(t) = \cos\theta_q^{\mathrm{PR}}(t). \tag{12}$$

The middle-left panel in Fig. 4 illustrates the four samples of the given epochs. The phases were locked at 0 s.

The bottom-left panel shows the conventional and phase-compensated average. While the conventional average revealed the stimulus-induced activity via the phase-reset, the phase-compensated average revealed the phase modulation of the phase-reset; the amplitudes of these averages changed complementarily, and therefore, the conventional average was not caused by stimulus-evoked, or additive, activities. These averages also revealed upward (duration B) and downward (duration C) shifts in frequency. These shifts were coincident with the given phases. Note that the time derivative of phase is frequency.

B. Baseline Shift

A third xEG generation model has been recently proposed [8]. In this model, the conventional average, or the mean time series, is stimulus-induced via an amplitude modulation of a baseline-shifted ongoing spontaneous activity.

The single-channel and 200-trial ($q = 0, 1, \ldots, 199$) xEG epochs follow

$$x_q^{\mathrm{BS}}(t) = (1 - \exp(-100t^2))(\cos\psi_q^{\mathrm{PR}}(t) - 0.5) \tag{13}$$

associated with equally spaced phases (11). BS stands for baseline shift. The top- and middle-right panels in Fig. 4 illustrate the given phases and epochs, respectively. The figures show an amplitude modulation rather than a phase modulation. The bottom-right panel shows the conventional and phase-compensated averages. Similar to the phase-reset simulation, the amplitudes of these averages changed complementarily, and therefore, the conventional average was not caused by the stimulus-evoked activities. However, unlike the phase-reset simulation, these averages successfully revealed the amplitude modulation but no phase modulation.

V. Results and Discussion

We applied this method to an offline analysis of a simple EEG experiment to determine whether information lost by using only conventional averaging can be recovered or not.

A. EEG Recording

Three subjects experienced three runs of flash stimuli, each of which consisted of 200 flashes (stimulus onset timing: 0 s, flash duration: 0.033 s, stimulus onset asynchrony: 2–3 s random). They received instructions just before each run; i.e., they were asked in Run 1) to view the flashes passively, in Run 2) to press a button as soon as they recognized the flashes, and in Run 3) to view them passively again. Thus, Runs 1–3 had no essential differences as stimuli and that Runs 1 and 3 were the same even with their instructions.

During these runs, 31-channel EEG (extended international 10–20 system) was simultaneously recorded with a sampling frequency of 1.2 kHz. Phase-compensated averaging used the same passbands, duration G, and timing n_0, as in Simulation I.

The subjects gave written informed consent after a detailed explanation of this study. The study received ethical approval from the Ethics Committee for Human and Animal Research of the Graduate School of Frontier Sciences, the University of Tokyo.

The scope of this paper is not to discuss brain functions but to describe a new averaging method. Hence, it is enough for our purpose to present an analysis of two-channel EEG (FCz: located at frontal point on the medial line, Oz: located at the occipital point on the medial line) for a typical subject.

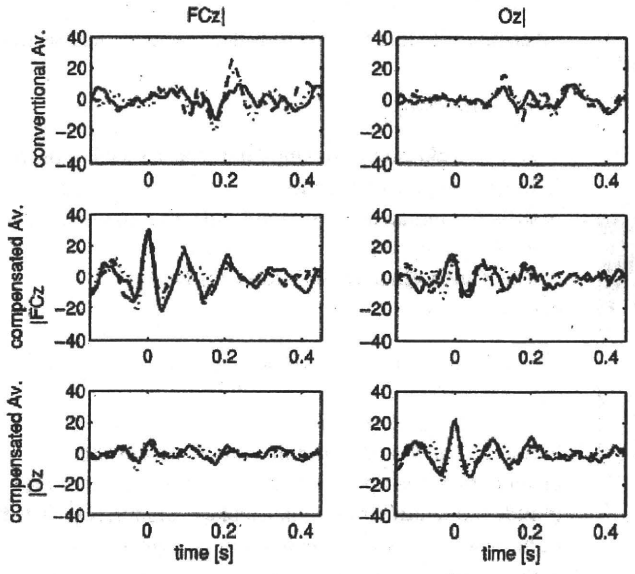

Fig. 5. Phase-compensated averages of a flash evoked potential. In all six panels, the dotted, dashed, and solid lines indicate EEG time series from Runs 1, 2, and 3, respectively. (left column) EEG time series of FCz (a frontal channel). (right column) EEG time series of Oz (an occipital channel). (top row) Conventional averages. (middle row) Averages compensated by instantaneous phases of FCz. (bottom row) Averages compensated by instantaneous phases of Oz.

B. Conventional Averages

The top-row of Fig. 5 shows conventional averages of FCz and Oz. For both channels, Run 2 showed a large activity and Run 3 showed a small activity relative to Run 1. The conventional averages of both channels for Run 3 were rather similar to those for Run 1 in terms of the waveform. This implies that button pressing and attention to this task increased activity in Run 2 and habituation decreased activity in Run 3. However, these speculations are not important; only amplitude and similarity relations among Runs 1–3 are relevant to our purpose.

C. Phase-Compensated Averages

The middle and bottom rows of Fig. 5 show compensated averages of FCz and Oz. The presentation style is the same as in Fig. 3.

The auto averages of both channels for Run 3 showed large activities. Moreover, the EEG time series of the auto averages for Run 3 were similar to those for Run 2 in terms of the waveform.

On the other hand, the cross averages of Oz compensated by FCz showed larger activities than those of FCz compensated by Oz. This implied that the directional relationship, or an information flow, from frontal (FCz) to occipital (Oz) was more prominent than from Oz to FCz. Although the reverse direction is believed to be a visual pathway, information flow from frontal to occipital has been also reported [6]. Putting the issue of the direction aside, we note that cross averages are useful for revealing such a directional relationship. Moreover, the auto averages of both channels for Run 3 were also similar to those for Run 2 in terms of the waveform.

Regarding the auto and cross averages, Run 3 had amplitude and similarity relations different from those obtained by only conventional averaging. This implies that information regarding Run 3 that cannot be explained by only habituation and may be affected by the experience of Run 2, was revealed by phase-compensated averaging. Note that the important point here is not speculation about brain functions but potential of this method to recover information.

D. Relationship Between Phase-Compensated Averages and Phase-Related Phenomena

As shown in the phase-compensated averages of channels 1 and 2 (see Fig. 3) and those of FCz and Oz (see Fig. 5), long-distance directional synchronizations were investigated by looking at the cross averages. Although we applied this method directly to EEG epochs to avoid a discussion nonessential to propose this method, this method can be applied to epochs that closely reflect brain activities (e.g., electrocorticogram (ECoG) and inverse solutions of xEG) without any modification.

If long-distance directional phase synchronization between two brain areas occurs, one must phase-synchronize to the other. In the meantime, a phase-reset must also occur. Note that phase-reset here does not mean the well-known phase-reset in which instantaneous phases jump to a specific value like in Simulation II, but rather a sort of drawing phenomenon that occurs between channels 1 and 2 in Simulation I. Phase-compensated averaging can detect both types of phase-reset.

Let us briefly discuss ERS/ERD because phase-compensated averaging does not directly visualize ERS/ERD. If the phase-reset similar to Simulation I occurs mainly in the alpha rhythms, the beta- and gamma-rhythms are generated in the transient phase-locking duration. These phenomena may be observed as ERS/ERD. In fact, a phase with a slope steeper than the alpha band appears in the top-right panel of Fig. 2.

The alpha-band activity often observed in phase-compensated averages, which in fact appears in Fig. 5, should be treated as a kind of alpha ringing. This is because alpha ringing is observed in conventional averages, which are interpreted as cross averages that are phase-compensated by the external trigger channel.

VI. Conclusion

We presented a complex-weighted averaging method, called phase-compensated averaging, to reveal amplitude and phase modulations of the target ongoing spontaneous activity, e.g., alpha rhythm. In this method, the instantaneous phases of xEG epochs at a specific time are first calculated. The specific time must be chosen such that the instantaneous phases are uniformly distributed from 0 to 2π. By making a suitable choice, the phase-compensated averages can reveal the modulations without the leakage of the purely stimulus-evoked activity while the conventional averages suffer from the leakage of the phase modulation. However, since the relationship between conventional averaging and phase-compensated averaging is complementary as shown in Simulations I and II, simultaneous use of these averages would be useful for analyzing the stimulus-evoked and/or stimulus-induced xEG activities. Note that we do not

infer the existence of the stimulus-evoked, or additive, activity. Moreover, phase-compensated averaging can reveal the directional phase synchronization between a pair of xEG channels. This characteristic would be useful for analyzing the directional relationship among xEG channels.

REFERENCES

[1] S. Makeig, M. Westerfield, T. P. Jung, S. Enghoff, J. Townsend, E. Courchesne, and T. J. Sejnowski, "Dynamic brain sources of visual evoked responses," *Science*, vol. 295, pp. 690–694, 2002.

[2] Y. Naruse, A. Matani, T. Hayakawa, and N. Fujimaki, "Influence of seamlessness between pre- and post stimulus alpha rhythms on visual evoked potential," *NeuroImage*, vol. 32, pp. 1221–1225, 2006.

[3] C. Tallon-Baudry and O. Bertrand, "Oscillatory gamma activity in humans and its role in object representation," *Trends Cognitive Sci.*, vol. 3, pp. 151–162, 1999.

[4] E. Rodriguez, N. George, J. P. Lachaux, B. Renault, and F. J. Varela, "Perception's shadow: long-distance synchronization of human brain activity," *Nature*, vol. 397, pp. 430–433, 1999.

[5] A. Brovelli, M. Ding, A. Ledberg, Y. Chen, R. Nakamura, and S. L. Bressler, "Beta oscillations in a large-scale sensorimotor cortical network: Directional influences revealed by Granger causality," *Proc. Natl. Acad. Sci.*, vol. 101, pp. 9849–9854, 2003.

[6] G. Nolte, A. Ziehe, V. V. Nikulin, A. Schlögl, A. Krämer, T. Brismar, and K. R. Müller, "Robustly estimating the flow direction of information in complex physical systems," *Phys. Rev. Lett.*, vol. 100, p. 234101, 2008.

[7] A. V. Oppenheim and R. W. Schafer, *Discrete-Time Signal Processing*, 2nd ed. Englewood Cliffs, NJ: Prentice-Hall, 1999.

[8] V. V. Nikulin, K. Linkenkaer-Hansen, G. Nolte, S. Lemm, K. R. Müller, R. J. Ilmoniemi, and G. Curio, "A novel mechanism for evoked responses in the human brain," *Eur. J. Neurosci.*, vol. 25, pp. 3146–3154, 2007.

[9] M. L. Van Quyen, J. Foucher, J. P. Lachaux, E. Rodriguez, A. Lutz, J. Martinerie, and F. J. Varela, "Comparison of Hilbert transform and wavelet methods for the analysis of neuronal synchrony," *J. Neurosci. Methods*, vol. 11, pp. 83–98, 2001.

Ayumu Matani (M'96) received the B.E., M.E., and Ph.D. degrees in control engineering from Osaka University, Osaka, Japan, in 1989, 1991, and 1998, respectively.

From 1991 to 1995, he was with Osaka Gas Company Ltd., and with Nara Institute of Science and Technology during 1995 through 1998. He is currently an Associate Professor at the Graduate School of Frontier Sciences, the University of Tokyo, Kashiwa, Japan, and an invited Researcher with the Biological ICT Group, National Institute of Information and Communication Technology, Kobe, Japan. His research interests include signal processing, complex system theory, and brain imaging.

Yasushi Naruse received the B.E. degree in mathematical engineering and information physics from the University of Tokyo, Tokyo, Japan, and the M.S. and Ph.D. degrees in complexity science and engineering from the University of Tokyo, Kashiwa, Japan, in 2002, 2004, and 2007, respectively.

He is currently an Expert Researcher with the Biological ICT Group, National Institute of Information and Communication Technology, Kobe, Japan. His research interests include signal processing and modeling of neural activities.

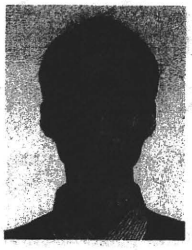

Yasushi Terazono received the B.E. and M.E. degrees in mathematical engineering and information physics, and the Ph.D. degree in complexity science and engineering from the University of Tokyo, Tokyo, Japan, in 1999, 2001, and 2004, respectively.

From 2004 to 2009, he was with National Institute of Information and Communication Technology, Kobe, Japan. He is currently a Postdoctoral Fellow with the Graduate School of Frontier Sciences, the University of Tokyo, Kashiwa. His research interests include inverse problems and mathematical programming.

Taro Iwasaki received the B.E. degree in mechanical engineering from Tokyo University of Science, Tokyo, Japan in 2008. He is currently working toward the M.S. degree at the Graduate School of Frontier Sciences, the University of Tokyo, Kashiwa, Japan.

His current research interests include signal processing for complex biological systems.

Norio Fujimaki (M'80) received the B.E., M.E., and Ph.D. degrees in electronics engineering from the University of Tokyo, Tokyo, Japan, in 1975, 1977, and 1980, respectively.

From 1980 to 1999, he was with Fujitsu Laboratories Ltd., Atsugi, Japan. He is currently a Senior Researcher with the Biological ICT Group, National Institute of Information and Communication Laboratory, Kobe, Japan (since 1999), a Visiting Professor with the Graduate School of Life Science and Systems Engineering, Kyushu Institute of Technology, Kitakyushu, Japan (since 2001), and with the Human Information System Laboratories, Kanazawa Institute of Technology, Kanazawa, Ishikawa, Japan (since 2005). His research interest is measurements of linguistic brain functions.

Tsutomu Murata received the B.S., M.S., and Ph.D. degrees in pharmaceutical sciences (biophysics of the brain) from the University of Tokyo, Tokyo, Japan, in 1985, 1987, and 1993, respectively.

From 1992 to 1998, he was with Kanazawa Institute of Technology, Kanazawa, Ishikawa, Japan. He is currently the Subleader of Biological ICT Group, National Institute of Information and Communication Laboratory, Kobe, Japan. His research interests include psychophysics and neuroscience of emergent visual recognition.

Phase-Interpolated Averaging for Analyzing Electroencephalography and Magnetoencephalography Epochs

Ayumu Matani*, *Member, IEEE*, Yasushi Naruse, Yasushi Terazono, Norio Fujimaki, *Member, IEEE*, and Tsutomu Murata

***Abstract*—Stimulus-locked averages of electroencephalography (EEG) and magnetoencephalography (MEG) epochs reveal characteristic waveforms. EEG/MEG generation models to have reconstruct such waveforms have been recently proposed. These models assume that evoked, phase-modulated, and amplitude-modulated activities occur solely or simultaneously. We propose a two-stage stimulus-locked averaging method, called phase-interpolated averaging, to investigate the EEG/MEG generation process. First, virtual EEG/MEG epochs, which would be obtained as if instantaneous phases for each time sampling point were on a phase-grid, are interpolated from actually measured EEG/MEG epochs. Then, the virtual EEG/MEG epochs are discrete Fourier transformed. A simulation revealed that the zeroth Fourier term revealed the evoked activity, the first Fourier term revealed the amplitude-modulated activity, and the condition number of the interpolation reflected the phase-modulated activity. On the basis of these facts, a preliminary EEG analysis implied that the evoked activity is much smaller than what would be expected by using conventional averaging, the evoked and phase-modulated activities simultaneously occur, and the amplitude-modulated activity occasionally associates with the evoked and phase-modulated activities. To the best of our knowledge, this is the first time that these three activities have been shown to coexist by actually separating them.**

***Index Terms*—Amplitude modulation, averaging, electroencephalography (EEG), evoked activity, magnetoencephalography (MEG), phase modulation, phase reset.**

I. Introduction

STIMULUS-LOCKED averages (conventional averages, hereafter) of electroencephalography (EEG) and magnetoencephalography (MEG) epochs have characteristic waveforms called the contingent negative variation (CNV), visual potential/field, Go potential/field, and NoGo potential/field, etc. [9].

EEG/MEG (xEG, hereafter) generation models to reconstruct such waveforms have been recently studied. The simplest model is the evoked model. An evoked activity common to all xEG epochs is added to ongoing rhythmic activities just like an impulse response. Since the evoked activity is stimulus-locked and ongoing rhythmic activities contrarily are not so in this model, the conventional average will converge to the evoked activity. Thus, most researchers who perform conventional averaging, regardless of whether they do it explicitly or implicitly, adopt the evoked model.

The second model is the phase-reset model [1]. The phase reset is a sort of phase modulation; instantaneous phases jump to a specific phase as a result of stimuli, and thereby the distribution of the instantaneous phases changes from uniform to biased. The conventional average reveals the waveform caused by this bias. There has recently been a debate about which of these models is correct [6] and the possibility of both of them coexisting has been pointed out [7]. Phase modulation, and temporal- and spatial-phase synchronization/desynchronization in the brain have also been pointed out [2]–[4], which means that the conventional average contains biases that the phase-related phenomena produce. A hypothesis relating the phase synchronization/desynchronization to the phase reset has been proposed [5].

A third xEG generation model [8] has been proposed. In this model, the conventional average is the result of an amplitude modulation of a baseline-shifted ongoing rhythmic activity.

The aforementioned models are based on one or more elementary processes: evoked (EV), phase-modulated (PM), and amplitude-modulated (AM) activities. Therefore, in order to investigate the xEG generation process, these elementary processes should be separately extracted from measured xEG epochs. However, only the evoked activity is additive, and this means separating them is not a simple task. In this paper, we propose a stimulus-locked averaging method, called phase-interpolated averaging, for this purpose.

II. Method

We begin by outlining an interpretation of phase-compensated averaging [5] that will lead us to phase-interpolated averaging.

Manuscript received June 8, 2010; revised July 30, 2010; accepted September 20, 2010. Date of publication September 30, 2010; date of current version December 17, 2010. This work was supported in part by a Grant-in-Aid for Scientific Research (B) (No. 21300102) from the Ministry of Education, Science, Sports and Culture. *Asterisk indicates corresponding author.*

*A. Matani is with Graduate School of Frontier Sciences, The University of Tokyo, Kashiwa 277-8561, Japan, and also with Biological ICT Group, National Institute of Information and Communication Technology, Kobe 651-2492, Japan (e-mail: matani@isp.ac).

Y. Naruse and T. Murata are with Biological ICT Group, National Institute of Information and Communication Technology, Kobe 651-2492, Japan (e-mail: y_naruse@po.nict.go.jp; benmura@po.nict.go.jp).

Y. Terazono is with Graduate School of Frontier Sciences, the University of Tokyo, Kashiwa 277-8561, Japan (e-mail: teraz@isp.ac).

N. Fujimaki is with Biological ICT Group, National Institute of Information and Communication Technology, Kobe 651-2492, Japan, with Graduate School of Life Science and Systems Engineering, Kyushu Institute of Technology, Kitakyushu 808-0196, Japan, and also with the Human Information System Laboratories, Kanazawa Institute of Technology, Kanazawa 921-8501, Japan (e-mail: fujimaki@po.nict.go.jp).

Color versions of one or more of the figures in this paper are available online at http://ieeexplore.ieee.org.

Digital Object Identifier 10.1109/TBME.2010.2081990

Note that phase-interpolated averaging is not a modification of phase-compensated averaging, since it has a different purpose.

A. Phase-Compensated Averaging

Phase-compensated averaging has been proposed as a way of evaluating the directional relationship between xEG channels. The autoaverage of phase-compensated averaging is outlined as follows. The xEG time series of a channel, qth epoch ($q = 0, 1, \ldots, Q-1$), and nth time sampling point is denoted by $x_q[n]$ ($n = 0$: stimulus onset timing). First, $x_q[n]$ is narrow-band filtered (e.g., alpha–beta band) and Hilbert transformed to get $\tilde{x}_q^{\mathrm{N}}[n]$. Second, the instantaneous phase $\mathrm{Arg}\{\tilde{x}_q^{\mathrm{N}}[n_0]\}$ at the time sampling point n_0 is calculated. Third, $x_q[n]$ is wide-band filtered (e.g., delta–gamma band) and Hilbert transformed to get $\tilde{x}_q^{\mathrm{W}}[n]$. Finally, the autoaverage of phase-compensated averaging is determined as

$$\bar{x}^{n_0}[n] = \frac{1}{Q}\sum_{q=0}^{Q-1} \tilde{x}_q^{\mathrm{W}}[n] \exp\left(-\mathrm{j}\mathrm{Arg}\left\{\tilde{x}_q^{\mathrm{N}}[n_0]\right\}\right), \quad (1)$$

where j is the imaginary unit. Thus, the wideband xEG epochs $\tilde{x}_q^{\mathrm{W}}[n]$ are averaged with their narrow-band instantaneous phase $\mathrm{Arg}\{\tilde{x}_q^{\mathrm{N}}[n_0]\}$ compensated to be zero. The autoaverage (1) evaluates how the phase alignment of the xEG epochs at n_0 maintains or decays over time, and it implicitly includes the phase-preservation index [11]. One can find that the conventional average

$$\bar{x}[n] = \frac{1}{Q}\sum_{q=0}^{Q-1} x_q^{\mathrm{W}}[n] \quad (2)$$

is the autoaverage (1) in the case of $\mathrm{Arg}\{\tilde{x}_q^{\mathrm{N}}[n_0]\} = 0$.

Let us consider a virtual case:

$$\mathrm{Arg}\{\tilde{x}_q^{\mathrm{N}}[n_0]\} = \frac{2\pi q'}{Q}, \qquad (q' = 0, 1, \ldots, Q-1). \quad (3)$$

Equation (3) means that all of the instantaneous phases $\mathrm{Arg}\{\tilde{x}_q^{\mathrm{N}}[n_0]\}$ are on different phase-grids $2\pi q'/Q$, where the map $q \mapsto q'$ is one-to-one. Under the grid-phase sampling condition (3), or no jitter condition, the autoaverage (1) will be the first term of the discrete Fourier transform. Although the conventional average (2) is apparently the zeroth Fourier term without the grid-phase sampling condition (3), this condition is necessary in order to truly call the conventional average the zeroth Fourier term in contrast to the first Fourier term. Moreover, on the basis of this Fourier aspect, the phase-sorted xEG epoch order q', which is completely different from the stimulus presentation number q, can be given a physical meaning in the same way that "time" and "channel" have physical meanings.

B. Procedure of Phase-Interpolated Averaging

Phase-interpolated averaging separately extracts the EV, PM, and AM activities. It is extremely unlikely for measured xEG epochs to satisfy the grid-phase sampling condition (3), even at a time sampling point. Phase-interpolated averaging consists of two stages: I) virtual xEG epochs satisfying the grid-phase sampling condition (3) are estimated by interpolating measured xEG epochs and 2) the virtual xEG epochs are discrete Fourier transformed. Stage II seeks to remove only PM, whereas stage II seeks to separately extract EV and AM from the residual signal. Note that unlike phase-compensated averaging: 1) only the wide band xEG epochs are necessary and 2) stages I and II are done for each time sampling point and for each xEG channel (only auto term). Note that "wideband xEG" (in contrast to "narrow-band xEG") is actually limited to a small range of less than 40–50 Hz (mainly the alpha and delta bands), and the sampling frequency is usually set at several hundreds hertz or higher. Therefore, objective xEG epochs can be generally regarded as narrow-band limited.

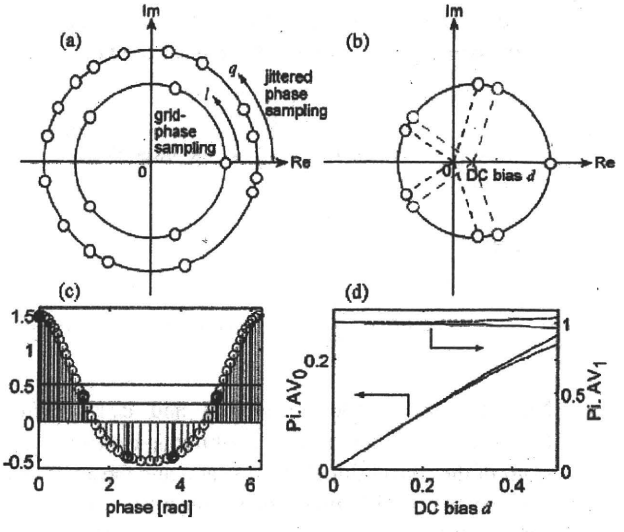

Fig. 1. Phase-interpolated averaging. (a) Concept of interpolation of phase sampling. Outer circle: Phase sampling. Instantaneous plots of measured xEG epochs having a constant amplitude on the complex plane can be treated as phase samples. Phase sampling always suffers from jitter. Inner circle: Virtual xEG epochs estimated by interpolating the measured xEG epochs. The interpolation resolves the phase-sampling jitters. (b) DC-bias problem of interpolation. Gray circles: Virtual xEG epochs estimated by interpolating about d. Black circles: Virtual xEG epochs estimated by interpolating about the axis origin. (c) Gray stems: Original 50-trial xEG epochs (dc bias $d = 0.5$) phase-sampled about the axis origin. Horizontal gray line: The mean of the original xEG epochs. Black stems: Virtual xEG epochs ($K = 2$). Horizontal black line: The mean of the virtual xEG epochs. (d) Zeroth and first phase-interpolated averages plotted versus dc bias d. These plots are used to compute multiplication coefficients η_0 and η_1.

1) Stage I (Interpolation): Fig. 1(a) shows the concept of interpolation. The outer circle illustrates instantaneous xEG epochs (complex-valued) on the complex plane; their amplitudes, or radii, are constant, for simplicity. Thus, this would be called phase sampling. Unlike time sampling, phase sampling is cropped from 0 to 2π and necessarily has a lot of sampling jitter; i.e., 2π is not equally divided. The inner circle illustrates phase sampling without jitter, namely grid-phase sampling.

The interpolation generates virtual xEG epochs satisfying the grid-phase sampling condition (3) from the measured xEG epochs on the basis of the periodic version of sampling theory, as follows. Let us consider phase sampling from continuous to discrete phases. The xEG time series of a channel, nth time sampling point, and continuous phase ψ is denoted by $x_n(\psi)$.

Since $x_n(\psi)$ is treated as periodic, $x_n(\psi)$ can be approximated by the partial sum up to $\pm K$th order of the Fourier series

$$x_n(\psi) \simeq \sum_{k=-K}^{K} c_n[k] \exp(\mathrm{j}k\psi), \tag{4}$$

where

$$c_n[k] = \frac{1}{2\pi} \int_{-\pi}^{\pi} x_n(\psi) \exp(-\mathrm{j}k\psi)\, \mathrm{d}\psi. \tag{5}$$

Note that $c_n[0]$ (dc amplitude) and $c_n[1]$ (fundamental-frequency amplitude) are the continuous Fourier transform versions of the conventional average at n and the autoaverage (1) at n, respectively. This indicates that these two terms, respectively, correspond to EV and AM (only fundamental term) without mutual leakage. If grid-phase sampling for $2K+1$ (from $-K$ to K) epochs is performed for $x_n(\psi)$, the discrete Fourier transform version of (5) is simply

$$c_n^{\mathrm{G}}[k] = \frac{1}{2K+1} \sum_{l=0}^{2K} x_n\left(\frac{2\pi l}{2K+1}\right) \exp\left(-\mathrm{j}\frac{2\pi kl}{2K+1}\right). \tag{6}$$

The superscript "G" stands for grid-phase sampling. Substituting (6) into (4), we get

$$\begin{aligned} & x_n(\psi) \\ & \simeq \sum_{k=-K}^{K} c_n^{\mathrm{G}}[k] \exp(\mathrm{j}k\psi) \\ & = \sum_{k=-K}^{K} \frac{1}{2K+1} \sum_{l=0}^{2K} x_n\left(\frac{2\pi l}{2K+1}\right) \exp\left(-\mathrm{j}\frac{2\pi kl}{2K+1}\right) \exp(\mathrm{j}k\psi) \\ & = \sum_{l=0}^{2K} x_n\left(\frac{2\pi l}{2K+1}\right) \frac{1}{2K+1} \sum_{k=-K}^{K} \exp\left(\mathrm{j}k\left(\psi - \frac{2\pi l}{2K+1}\right)\right) \\ & = \sum_{l=0}^{2K} x_n\left(\frac{2\pi l}{2K+1}\right) \mathrm{diric}_{2K+1}\left(\psi - \frac{2\pi l}{2K+1}\right), \end{aligned} \tag{7}$$

where

$$\mathrm{diric}_{2K+1}(\psi) = \frac{\sin((2K+1)\psi/2)}{(2K+1)\sin(\psi/2)}. \tag{8}$$

is the Dirichlet kernel of the $2K+1$th order. Equation (7) corresponds to the periodical version of sampling theory.

Now, let us turn to the jittered sampling case, which is not so simple. By using the Fourier series (7), the phase-sorted q'th xEG epoch having phase-sampling jitters can be calculated as

$$\boldsymbol{x}_n^{\mathrm{J}} \simeq \Xi_n \boldsymbol{x}_n^{\mathrm{G}}, \tag{9}$$

where

$$\begin{aligned} \boldsymbol{x}_n^{\mathrm{J}} &= [x_n(\psi_n^{\mathrm{J}}[0]) \cdots x_n(\psi_n^{\mathrm{J}}[q']) \cdots x_n(\psi_n^{\mathrm{J}}[Q-1])]^{\mathrm{T}}, \\ \boldsymbol{x}_n^{\mathrm{G}} &= \left[x_n(0) \cdots x_n\left(\frac{2\pi l}{2K+1}\right) \cdots x_n\left(\frac{2\pi K}{2K+1}\right)\right]^{\mathrm{T}}, \\ \Xi_n &= [\xi_{xq'l}], \quad \xi_{xq'l} = \mathrm{diric}_{2K+1}\left(\psi_n^{\mathrm{J}}[q'] - \frac{2\pi l}{2K+1}\right). \end{aligned} \tag{10}$$

The superscript "J" stands for jittered phase sampling. Note that $\psi_n^{\mathrm{J}}[q']$ is calculated by using the epochwise discrete Hilbert transform; i.e., $\psi_n^{\mathrm{J}}[q']$ is only here treated as a function of n. See the Appendix for a discussion of the underdeterminedness of $\psi_n^{\mathrm{J}}[q']$.

By setting K such that $2K+1 < Q$, which means a reduction in the number of xEG epochs, we can estimate x_n^{G} in the least squares sense as

$$\hat{\boldsymbol{x}}_n^{\mathrm{G}} = \left[\Xi_n^{\mathrm{T}}\Xi_n + \lambda^2 \mathbf{I}_{2K+1}\right]^{-1} \Xi_n^{\mathrm{T}} \boldsymbol{x}_n^{\mathrm{J}}, \tag{11}$$

where $\mathbf{I}_{2K+1}$ is the $2K+1$th unit matrix and λ^2 is a regularization parameter. Thus, we obtain the virtual xEG epoch $\hat{\boldsymbol{x}}_n^{\mathrm{G}}$. The condition number of Ξ_n in (10) indicates the difficulty of the interpolation, and therefore, it also qualitatively reflects PM. The optimal K (interpolation order) and λ^2 will be computed in Section III-E.

2) Stage II (Discrete Fourier Transform): Here, we are interested in only the zeroth and the real part of the first Fourier terms; the estimate of $c_n^{\mathrm{G}}[0]$ is called the zeroth phase-interpolated average and that of $2\mathrm{Re}\{c_n^{\mathrm{G}}[1]\} = c_n^{\mathrm{G}}[1] + c_n^{\mathrm{G}}[2K]$ is called the first phase-interpolated average. Stage II estimates $c_n^{\mathrm{G}}[0]$ and $2\mathrm{Re}\{c_n^{\mathrm{G}}[1]\}$ of (6) by taking the discrete Fourier transform of the virtual xEG epoch $\hat{\boldsymbol{x}}_n^{\mathrm{G}}$. The reason the first phase-interpolated average is not simply the estimate of $c_n^{\mathrm{G}}[1]$ is that $\hat{\boldsymbol{x}}_n^{\mathrm{G}}$ is real-valued. These two averages are, respectively, expressed as

$$\begin{aligned} \bar{x}_0[n] &= \frac{\eta_0}{2K+1} \sum_{l=0}^{2K} \hat{x}_n^{\mathrm{G}}\left(\frac{2\pi l}{2K+1}\right), \\ \bar{x}_1[n] &= \frac{\eta_1}{2K+1} \mathrm{Re}\left\{\sum_{l=0}^{2K} \hat{x}_n^{\mathrm{G}}\left(\frac{2\pi l}{2K+1}\right) \exp\left(-\mathrm{j}\frac{2\pi l}{2K+1}\right)\right\}, \end{aligned} \tag{12}$$

where η_0 and η_1 are the multiplier coefficients, which will be computed in Section II-C. Note that only $\bar{x}_0[n]$ and $\bar{x}_1[n]$ are objectives of interest at the moment, and therefore, a whole calculation of the discrete Fourier transform is not necessary.

C. Multiplier Coefficients η_0 and η_1

Since the zeroth and first phase-interpolated averages $\bar{x}_0[n]$ and $\bar{x}_1[n]$ of (12) are the estimates of $c_n^{\mathrm{G}}[0]$ and $2\mathrm{Re}\{c_n^{\mathrm{G}}[1]\}$ of (6), respectively, one may think that the multiplier coefficients η_0 and η_1 in (12) should be set to 1 and 2 accordingly. However, these values are correct, only if the instantaneous phases are calculated without a dc bias. This dc bias is what the evoked

model is about. Therefore, η_0 and η_1 are used for compensation of the dc bias.

Let us explain the dc bias problem and compute appropriate η_0 and η_1 in (12). Suppose that there is a continuous one-periodic sinusoid having unit amplitude with an unknown dc bias d and the original 50-trial xEG epochs are obtained by phase sampling the sinusoid under condition (3) about d; i.e., grid-phase sampling is performed with d as its center. The gray circles of Fig. 1(b) show virtual xEG epochs estimated by interpolating the original xEG epochs about d. The interpolation is almost identical to simple resampling in this case. The mean of the original xEG epochs is, of course, d, and that of the virtual xEG epochs is also d. Note that the situation up to this point is the same as in Fig. 1(a) because the dc bias does not affect the situation.

However, the actual interpolation is performed not about an unknown dc bias, but about the axis origin, as shown by the black circles in Fig. 1(b). The gray stems, i.e., the gray lines with circles, of Fig. 1(c) show the original xEG epochs phase-sampled about the axis origin (dc bias $d = 0.5$). Phase-sampling jitters occur, but the grid-phase sampling condition (3) will be satisfied if it is done about $d = 0.5$. The mean of the original xEG epochs, which is shown by the horizontal gray line, is still d. On the other hand, the black stems indicate the virtual xEG epochs ($K = 2$). The virtual xEG epochs seem to be properly placed as interpolations. However, the mean of the virtual xEG epochs, i.e., the horizontal black line, is not d because of the resolved phase-sampling jitters. Therefore, η_0 in (12) should not be set to 1. Similarly, η_1 should also be recomputed.

Fig. 1(d) shows the zeroth and first phase-interpolated average changes (stacked for $K = 1, 2, \ldots, 6$ in (6), tentatively, $\eta_0 = 1$ and $\eta_1 = 2$) versus d. Note that these averages, except those of $K = 1$ (dashed lines), overlap. Although there are slight differences with different K, the zeroth phase-interpolated averages are roughly $d/2$ and the first ones are roughly 1 independent of d. Therefore, $\eta_0 = 2$ and $\eta_1 = 2$ are employed accordingly.

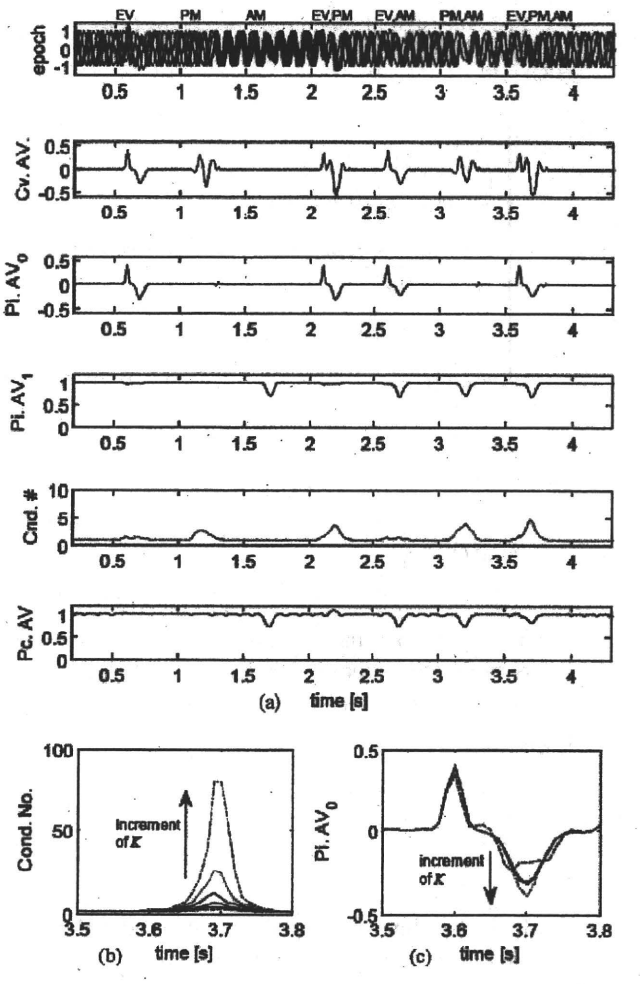

Fig. 2. Simulation of phase-interpolated averaging. (a) Top row: Five samples ($q = 0$, 10, 20, 30, and 40) of the given 50-trial xEG epochs. Second row: Conventional average. Third row: Zeroth phase-interpolated average ($K = 3$). Fourth row: First phase-interpolated average ($K = 3$). Fifth row: Condition number ($K = 3$). Bottom row: Phase-compensated average. (b) Change in condition number for a duration of 3.5–3.8 s with increment of $K = 1, 2, \ldots, 6$ (from bottom to top, broken lines: $K = 1$, 6). (c) Change in zeroth phase-interpolated average for a duration of 3.5–3.8 s with increment of $K = 1, 2, \ldots, 6$ (from top to bottom, broken lines: $K = 1$, 6). The simulation had a sampling frequency of 100 Hz.

III. Simulation

Phase-interpolated averaging is a means of investigating the xEG generation process. Even if three xEG activities (EV, AM, and PM) do not solely occur, phase-interpolated averaging should separate them as if each of them occurred solely. We performed a simulation to evaluate the separation ability of phase-interpolated averaging. Note that we did not have any prior hypothesis that these xEG activities occurred solely or simultaneously.

A. Given Epochs

Single-channel and 50-trial xEG epochs $x_q(t)$, $(q = 0, 1, \ldots, 49, 0 \le t \le 4.5\,\text{s})$ were given as

$$x_q(t) = x^{\text{EV}}(t) + a_q^{\text{AM}}(t)\cos\theta_q^{\text{PM}}(t), \tag{13}$$

where $x^{\text{EV}}(t)$ was the EV, $a^{\text{AM}}(t)$ was the AM, and $\theta_q^{\text{PM}}(t)$ was the epoch-wise PM. Note that AM and PM are not simply superimposed. The top row of Fig. 2(a) shows five samples of $x_q(t)$. EV, PM, and AM solely or simultaneously occurred in durations of $t \in [0.5u,\ 0.5u + 0.3]$, $(u = 1, 2, \ldots, 7)$. EV, PM, and AM were set as follows.

EV consisted of two Gaussian functions

$$x^{\text{EV}}(t) = \begin{cases} 0.4\exp(-5\cdot 10^3(t-(0.5u+0.1))^2) \\ \quad -0.3\exp(-10^3(t-(0.5u+0.2))^2), & u = 1, 4, 5, 7 \\ 0, & \text{otherwise.} \end{cases} \tag{14}$$

PM consisted of random phase connections [5]

$$\theta_q^{\mathrm{PM}}(t) = \begin{cases} \psi_{q(u-1)}(t), & 0.5u \le t \le 0.1 + 0.5u \\ \begin{pmatrix} \psi_{qu}(0.3 + 0.5u) \\ -\psi_{q(u-1)}(0.1 + 0.5u) \end{pmatrix} \cdot \left(\dfrac{t - 0.1 + 0.5u}{0.2}\right) & 0.1 + 0.5u < t \le 0.3 + 0.5u \\ \quad + \psi_{q(u-1)}(0.1 + 0.5u), & \\ \psi_{qu}(t), & 0.3 + 0.5u < t < 0.5u, \end{cases} \tag{15}$$

where

$$\psi_{qu}(t) = \begin{cases} 2\pi \cdot 10t + \dfrac{2\pi P_u[q]}{50}, & u = 2, 4, 6, 7 \\ 2\pi \cdot 10t + \dfrac{2\pi P_{u-1}[q]}{50}, & \text{otherwise} \end{cases} \tag{16}$$

and $P_u[q]$ denotes the random permutation of the integer numbers from 0 to 49 for the uth duration and $P_0[q] = q$.

AM consisted of a Gaussian envelope:

$$a^{\mathrm{AM}}(t) = \begin{cases} 1 - 0.3\exp(-10^3(t - (0.2 + 0.5u))^2), & u = 3, 5, 6, 7 \\ 1, & \text{otherwise.} \end{cases} \tag{17}$$

If the baseline shift and amplitude modulation model [8] is taken into account, (13) should be modified into

$$\begin{aligned} x'_q(t) &= a'^{\mathrm{AM}}(t)\left(x^{\mathrm{EV}}(t) + \cos\theta_q^{\mathrm{PM}}(t)\right) \\ &= a'^{\mathrm{AM}}(t)x^{\mathrm{EV}}(t) + a'^{\mathrm{AM}}(t)\cos\theta_q^{\mathrm{PM}}(t). \end{aligned} \tag{18}$$

Therefore, this model is already included in (13) when EV is also amplitude-modulated.

B. Conventional Averages

The second row of Fig. 2(a) shows the conventional average. EV and PM each generated activity, and the EV activity was superimposed on the PM activity when they simultaneously occurred. Thus, when the conventional average is not zero, it is impossible to identify which of only EV, only PM, or both EV and PM occurred.

C. Phase-Interpolated Averages

Phase-interpolated averaging was performed for $K = 3$. The third row of Fig. 2(a) shows the zeroth phase-interpolated average. Even if EV occurs with PM and/or AM, the zeroth phase-interpolated average quantitatively extracted only EV. The fourth row of Fig. 2(a) shows the first phase-interpolated average. The first phase-interpolated average quantitatively extracted the envelope of only AM. The fifth row of Fig. 2(a) shows the condition number of Ξ_n in (10). It qualitatively reflected the biased distributions of the instantaneous phases caused by only PM. Therefore, we can say that phase-interpolated averaging successfully separated EV, PM, and AM.

Let us briefly compare phase-interpolated averaging and conventional time-series analyses, such as the complex wavelet transform and Hilbert transform. One may think that the absolute values of the complex wavelet transform and the Hilbert transform of an xEG epoch can be used to estimate AM. However, these transforms produce nonzero activity even in the EV-only case: $x_q(t) = x^{\mathrm{EV}}(t)$, and thereby, they cannot separate EV and AM.

D. Phase-Compensated Averages

The bottom row of Fig. 2(a) shows the phase-compensated average in which xEG epochs (13) were used for both the narrow- and wideband xEGs. Although phase-compensated averaging has no notion of the zeroth and first averages, let it suffice here to say that the zeroth and first averages, respectively, correspond to the conventional [because of (2) and (12)] and incomplete first phase-interpolated (in the meaning that phase-compensated averaging led to the phase-interpolated average in Sections II-A and II-B) averages.

The zeroth phase-compensated average shows PM-contaminated EV. The first phase-compensated average showed EV–PM-contaminated AM (e.g., 2.1–2.3 s). Moreover, phase-compensated averaging is not able to detect PM separately. Therefore, the interpolation, which is the main difference between phase-compensated and phase-interpolated averaging, is necessary for the separation. Note that the purpose of phase-compensated averaging is not separation, but rather analysis of cross-channel directional synchronization.

E. Optimal Interpolation Order K and Regularization Parameter λ^2

Theoretically speaking, the larger the K is, the more accurate the interpolation will be. However, a much larger K should also make the condition number of the interpolation much larger. A very large K would thus degrade the accuracy of the interpolation. The reason the accuracy of the interpolation depends on K because the Fourier series (7) with interpolation (11) is not an orthogonal expansion.

Let us compute the optimal K and the regularization parameter λ^2. Fig. 2(b) shows the condition numbers for $K = 1, 2, \ldots, 6$ for a duration of 3.5–3.8 s for which EV, PM, and AM simultaneously occurred in the simulation. As expected, the condition number increased with the increment of K. Fig. 2(c) shows the zeroth phase-interpolated averages ($K = 1, 2, \ldots, 6$). They mostly overlapped for $K = 2, 3, \ldots, 5$, and EV was robustly and accurately reconstructed as (14) in this range of K. Fig. 2(b) and (c) roughly indicates that the upper bound of the condition number κ^{sup} for yielding an upper bound of K for accurate interpolation is about 20 or 30.

κ^{sup} can also help us to set λ^2 in (11). Note that λ^2 is only for stabilizing the pseudo inverse of Ξ_n. Too much stabilization degrades the accuracy of the interpolation to the extent that EV and PM cannot be separated. Thus, λ^2 should be set less than $(s^{\max}/\kappa^{\mathrm{sup}})^2$, where $s^{\max}$ is the maximum singular value of Ξ_n.

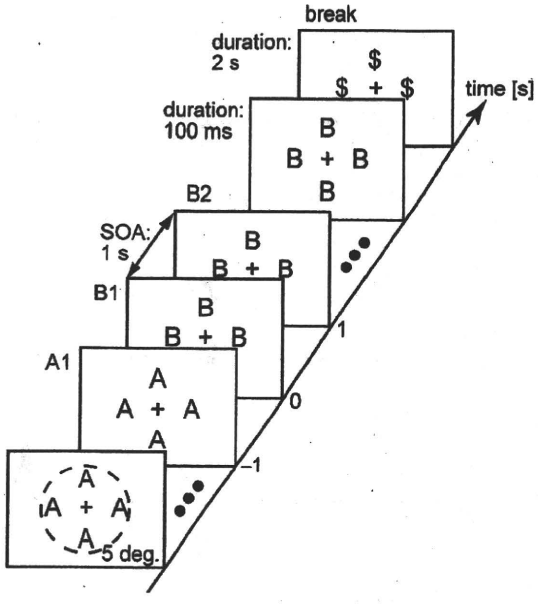

Fig. 3. Schematic diagram of the button-pressing experiment. 320 stimulus sequences, each of which consisted of A-images first, then B-images, and finally a $-image (eight images in total), was presented (40 sequences × 8 runs). The total number of A- and B-images was 7, and the number of A-images randomly changed from 1 to 5. Each image consisted of four A, B, or $ characters surrounding the fixation point + within 5° of visual angle. Each of the A- or B-images was displayed for 100 ms, and the stimulus onset asynchrony (SOA) was 1 s. The $-image was displayed at the end of every stimulus sequence for a 2-s break (e.g., for blinking). Subjects were instructed to press a button as soon as they saw the first B-image (B1).

For instance, κ^{sup} indicates that $(s^{\max}/100)^2$ would be a better choice for λ^2, and this is the value we employed.

In practice, phase-interpolated averaging should be performed for several Ks by referencing the changes in the condition number and ensuring the robustness of the averaging results.

IV. Results and Discussion

The good simulation results encouraged us to conduct phase-interpolated averaging on experimentally measured EEG epochs.

A. EEG Recording

Six subjects (Subjects 1–6) participated in a button-pressing experiment during which EEG recordings were made. Fig. 3 shows a schematic diagram of the experiment. The subjects were instructed to look at 320 stimulus sequences, each of which consisted of eight serially presented images (A-images, then B-images, and finally a $-image), and to press a button immediately when they saw the first B-image, which appeared with an unknown timing. In the stimulus sequences, the first B-image was symbolically called "B1" (onset: 0 s), the second B-image was called "B2" (onset: 1 s), and the A-image just preceding B1 was called "A1" (onset: −1 s). Thirty-one channels of EEG (extended international 10–20 system) were simultaneously recorded during the experiment (sampling frequency: 600 Hz). The reason we performed such a complex experiment was that we expected various potentials, e.g., visual (V), CNV, NoGo, and Go, to be included in the EEG epochs for A1, B1, and B2. Note that we excluded the EEG epochs where A1 was the first presented image in the stimulus sequences from further analysis for the reason explained in Section IV-B.

As preprocessing, EEG epochs having artifacts (e.g., blinking) in the duration to be analyzed and mistakes for button-pressing were eliminated and the remaining EEG epochs were bandpass filtered (with a finite impulse response filter: 1–50 Hz, 240th order). The valid EEG epochs numbered 251, 254, 252, 267, 269, and 261 for Subjects 1–6, respectively. The scope of this paper is not to discuss brain functions, but to describe a new averaging method and to investigate EEG generation processes. Hence, it is enough for our purpose to present an analysis of two-channel EEG (FC_z: located at frontal point on the medial line, O_z: located at the occipital point on the medial line).

The subjects gave written informed consent after they were given a detailed explanation of this study. The study received approval from the Ethics Committee for Human and Animal Research, Graduate School of Frontier Sciences, the University of Tokyo.

B. Conventional Averages

The thick gray lines in the top rows of Fig. 4(a) (FC_z) and (b) (O_z) show the conventional averages of Subject 1. The A1, B1, and B2 onsets are indicated on the horizontal axes. V potentials were observed for A1, B1, and B2 at FC_z and O_z for a duration of 100–250 ms after the stimulus onset. These V potentials could be simply caused by individual visual stimuli. CNV potentials were observed for A1 and B1 at FC_z in the pretrigger duration. These CNV potentials could be caused by the subject expecting the first B-image's appearance. In fact, a CNV potential was not observed for B2. The reason we excluded some of the EEG epochs prior to the analysis was that subjects did not seem to generate CNV for the first A-images, which were necessarily presented before the others. A NoGo potential was observed for A1 at FC_z for a duration of 200–500 ms after the stimulus onset. No NoGo potential was observed for B2, for which button-pressing was not necessary. A Go potential was observed for B1 at FC_z and also a part of that was observed at O_z for a duration of 200–500 ms after the stimulus onset. All of these potentials partially overlapped and may have included other event-related potentials, e.g., an attention-related one.

Subjects 2–6 showed very similar conventional averages. Table I summarizes the conventional averages of Subjects 1–6. The number of "+"s and the number in parentheses indicate a somewhat subjective amplitude of the activity and how many subjects showed such activity, respectively.

C. Phase-Interpolated Averages

The lines, except the thick gray ones, in Fig. 4 show the phase-interpolated averaging results of Subject 1. Fig. 4(c) (FC_z) and (d) (O_z) are the magnified views of Fig. 4(a) (FC_z) and (b) (O_z), respectively. The thin dashed, thin solid, and thin dash-dotted

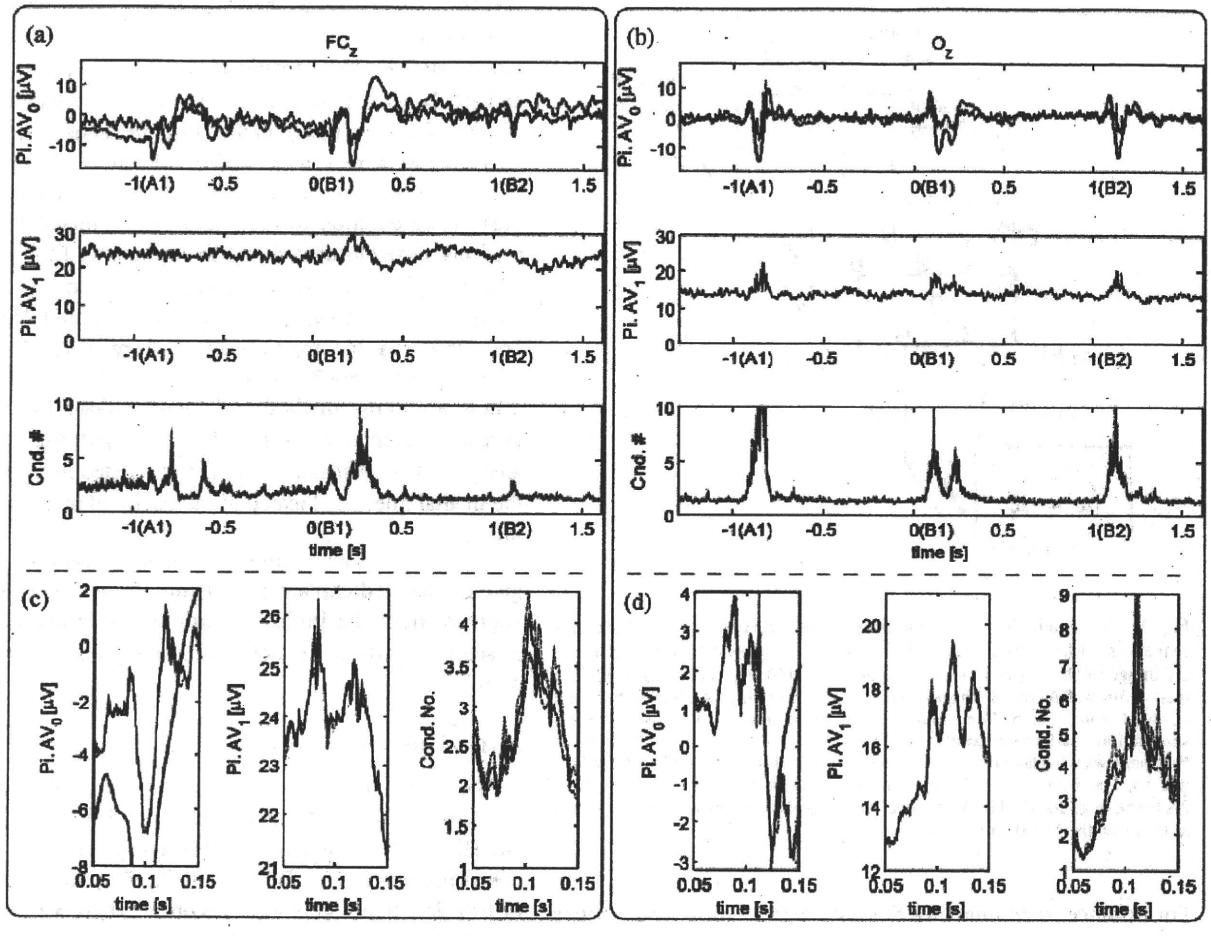

Fig. 4. Phase-interpolated averaging results of recorded EEGs [(a) and (c): FC_z; (b) and (d): O_z). Top rows of (a) and (b) Thick gray lines: conventional averages. Thin lines: zeroth phase-interpolated averages. Middle rows of (a) and (b) First phase-interpolated averages. Bottom rows of (a) and (b) Condition numbers. (c) and (d) Magnified views of (a) and (b) (0.05–0.15 s). Although the thin dashed, thin solid, and thin dash-dotted lines correspond to results for $K = 3$, 4, and 5, respectively, in all the plots, they mostly overlap, especially the zeroth and first phase-interpolated averages.

TABLE I
CONVENTIONAL AVERAGES OF SUBJECTS 1–6

electrode	duration	V	CNV	NoGo	Go
FCz	A1	++(6)	++(6)	++(5)	
	B1	++(5)	++(6)		+++(6)
	B2	++(5)			
Oz	A1	+++(5)		+(3)	
	B1	+++(5)			++(5)
	B2	+++(5)			

TABLE II
ZEROTH PHASE-INTERPOLATED AVERAGES OF SUBJECTS 1–6

electrode	duration	V	CNV	NoGo	Go
FCz	A1	+(4)	+(5)	+(5)	
	B1	+(5)	+(5)		++(5)
	B2	+(4)			
Oz	A1	++(3)			
	B1	++(4)			+(2)
	B2	++(3)			

lines correspond to results for $K = 3$, 4, and 5, respectively. The top, middle, and bottom rows of Fig. 4(a) and (b) correspond to the zeroth phase-interpolated averages, the first phase-interpolated averages, and the condition numbers of the interpolation, respectively. The zeroth and first phase-interpolated averages (three textured lines) mostly overlapped for the range of K, although a spiky disturbance was only seen for $K = 5$ in the left panel of Fig. 4(d). Thus, the overlapped phase-interpolated averages were somewhat reliable because they were similar to the simulation results [Fig. 2(c)].

The zeroth phase-interpolated averages showed 1) V potentials for A1, B1, and B2 at FC_z and O_z; 2) CNV potentials for A1 and B1 at FC_z; 3) a NoGo potential for A1 at FC_z; and 4) a Go potential for B1 at FC_z and also a part of that at O_z. All of the zeroth phase-interpolated averages were very similar to the conventional averages. However, their amplitudes were smaller than those of the conventional averages. The first phase-interpolated averages at O_z increased in the durations in which the V potentials were observed, and those at FC_z increased in the durations in which the Go potential was observed. The condition numbers at FC_z and O_z increased in the durations in which the V, part of NoGo, and Go potentials were observed.

Tables II–IV summarize the zeroth phase-interpolated averages, the first phase-interpolated averages, and the condition

TABLE III
FIRST PHASE-INTERPOLATED AVERAGES OF SUBJECTS 1–6

electrode	duration	V	CNV	NoGo	Go
FCz	A1				
	B1	+(1)			+(3)
	B2				
Oz	A1	+(5)			
	B1	+(5)			+(1)
	B2	+(4)			

TABLE IV
CONDITION NUMBERS OF SUBJECTS 1–6

electrode	duration	V	CNV	NoGo	Go
FCz	A1	+(6)	+(5)	++(5)	
	B1	+(6)	+(5)		++(6)
	B2	+(6)			
Oz	A1	++(6)		+(3)	
	B1	++(6)			++(6)
	B2	++(6)			

numbers of the interpolation, respectively, of Subjects 1–6. These presentation styles are the same as used for Table I.

D. EEG Generation Process

Let us briefly discuss the EEG generation characteristics common to the six subjects as a preliminary result. Tables I and II reveal that EV activities are smaller, occasionally vanishingly smaller, than the values estimated by using conventional averaging, but they highly probably exist. Tables II and IV indicate that EV and PM activities probably occur simultaneously and their ratio would vary as the case may be. The results in Tables II–IV suggest that AM activities occasionally associate with EV and PM activities and might modify the EV and PM activities. Consequently, the aforementioned aspects can be summed up that EV and PM models (including the phase reset model) coexist and the AM model (including the baseline shift and amplitude modulation model) occasionally occurs.

Finally, we should also consider that xEG-detectable activities in a single epoch are caused by the amount of the spatial synchronization of a huge number of neurons. The spatial synchronization in a single epoch might be a factor preventing us from making an unequivocal decision about the xEG generation process. The spatial synchronization in a single epoch would have EV-, AM-, and/or PM-like characteristics. Phase-interpolated averaging can investigate the spatial synchronization in a single epoch by substituting each neural activity for an xEG epoch; however, there is no method to measure tens of thousands of individual neurons noninvasively.

V. CONCLUSION

We presented a two-stage averaging method for xEG epochs, called phase-interpolated averaging, to separately investigate EV, PM, and AM activities. The first stage is the interpolation of xEG epochs as if grid-phase sampling were possible, and the second stage is a discrete Fourier transform of the interpolated xEG epochs. Phase-interpolated averaging separately extracts EV as the zeroth Fourier term, separately extracts the envelope of AM as the real part of the first Fourier term, and separately evaluates PM as the condition number of the interpolation. The results of a simulation and an EEG experiment using this method implied that 1) EV is much smaller than what would be with conventional averaging; 2) EV and PM activities simultaneously occur; and 3) AM activity occasionally associates with EV and PM activities. To the best of our knowledge, this is the first time that the coexistence of these three activities has been confirmed by actually separating them.

APPENDIX
UNDERDETERMINEDNESS OF INSTANTANEOUS PHASE GENERATION

Let us denote the discrete Fourier transform (DFT) and its inverse (DFT^{-1}) by using lower- and uppercases as follows:

$$X[k] = \mathrm{DFT}\{x[n]\},$$
$$x[n] = \mathrm{DFT}^{-1}\{X[k]\}, (n, k = 0, 1, \ldots, N-1). \quad \text{(A1)}$$

Complex-valued sequence $\tilde{x}[n]$ generation from a real-valued sequence $x[n]$ is based on at least the following two constraints. The first constraint is $x[n]$ and the real part of $\tilde{x}[n]$ are the same

$$x[n] = \mathrm{Re}\{\tilde{x}[n]\}. \quad \text{(A2)}$$

The second constraint is that they satisfy the symmetry relationships of the discrete Fourier transform

$$\begin{aligned}
\mathrm{DFT}\{\mathrm{ReEv}\{\tilde{x}[n]\}\} &= \mathrm{ReEv}\{\tilde{X}[k]\},\\
\mathrm{DFT}\{\mathrm{ReOd}\{\tilde{x}[n]\}\} &= \mathrm{ImOd}\{\tilde{X}[k]\},\\
\mathrm{DFT}\{\mathrm{ImEv}\{\tilde{x}[n]\}\} &= \mathrm{ImEv}\{\tilde{X}[k]\},\\
\mathrm{DFT}\{\mathrm{ImOd}\{\tilde{x}[n]\}\} &= \mathrm{ReOd}\{\tilde{X}[k]\}, \quad \text{(A3)}
\end{aligned}$$

where Re, Im, Ev, and Od stand for the real, imaginary, even function, and odd function parts, respectively. For instance, $\mathrm{ReEv}\{\cdot\}$ means the real and even function part of the sequence in the parenthesis. $\tilde{x}[n]$ and $\tilde{X}[n]$ in the top two rows of (A3) can be replaced with $x[n]$ and $X[n]$, because of (A2). Since there is no information for the bottom two rows of (A3), complex-valued signal generation requires an additional constraint. The discrete Hilbert transform generates the analytic sequence:

$$\tilde{x}[n] = \mathrm{DFT}^{-1}\{X[k]\,F[k]\}, \quad \text{(A4)}$$

in which the constraint is expressed as

$$F[k] = \begin{cases} 1, & k = 0, \dfrac{N}{2} \\ 2, & k = 1, 2, \ldots, \dfrac{N}{2} - 1 \\ 0, & k = \dfrac{N}{2} + 1, \dfrac{N}{2} + 2, \ldots, N-1 \end{cases} \quad \text{(A5)}$$

and N is an even number, for simplicity [10], [12]. $F[k]$ makes the negative frequency terms, which are actually thevadjust last

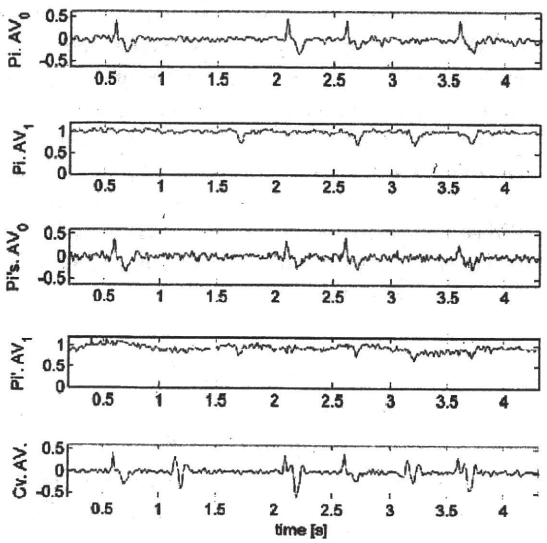

Fig. 5. Influence of the underterminedness of the discrete Hilbert transform on phase-interpolated averaging with noise. Top two rows: Zeroth and first phase-interpolated averages with the normal discrete Hilbert transform (with $F[k]$). Middle two rows: Zeroth and first phase-interpolated averages with an alternative discrete Hilbert transform (with $F'[k]$). Bottom row: Conventional average.

half of $X[k]$, zero. $F[k]$ also conserves the polarity-independent power spectrum

$$|X[k]|^2 + |X[N-k]|^2 = |\tilde{X}[k]|^2 + |\tilde{X}[N-k]|^2, \quad \left(k = 1, \ldots, \frac{N}{2} - 1\right). \quad \text{(A6)}$$

To satisfy (A2) and (A6), $F'[k]$ exists as an alternative to $F[k]$. $F'[k]$ treats negative frequency terms differently. One can swap 2 and 0 between $F[k]$ and $F[N-k]$; e.g., when $F[k]$ is [1 2 2 2 1 0 0 0], $F'[k]$, such as [1 0 2 2 1 0 0 2] and [1 2 0 0 1 2 2 0], can be used instead. In general, there are a total of $2^{N/2-1}$ variations.

Equation (A4) for each variation of $F'[k]$ generates a different $\mathrm{Im}\{\tilde{x}[n]\}$ and the same $\mathrm{Re}\{\tilde{x}[n]\}$. The $\tilde{x}[n]$s associated with $F'[k]$s are distributed on the horizontal line (A2) on the complex plane (symmetry about the real axis). $|\tilde{x}[n]|$ and $\mathrm{Arg}\{\tilde{x}[n]\}$ are thus underdetermined. In particular, if $X[k]$ is wideband, the distribution is accordingly wide. The phase interpolation based on $\mathrm{Arg}\{\tilde{x}[n]\}$ (11) is affected by this underdeterminedness. A different criterion must be necessary to deal with the underdeterminedness.

The first and second rows of Fig. 5 show the zeroth and first phase-interpolated averages with $F[k]$ for the simulated xEG epoch (13) with Gaussian noise (mean: 0, standard deviation: 0.25) added to widen the frequency band. The third and fourth rows show the phase-interpolated averages with an example of $F'[k]$ (randomly generated). The bottom row shows the conventional average. Although the phase-interpolated averages with $F[k]$ had a noise level similar to that of the conventional average, those with $F'[k]$ suffered from additional low- and high-frequency noise. Such additional noise, especially high-frequency noise, was observed even in the noise-free case and/or with a different $F'[k]$. Therefore, $F[k]$ is appropriate for phase-interpolated averaging.

$F[k]$ has another useful characteristic. Equation (A3) indicates that $\mathrm{DFT}^{-1}\{\mathrm{Od}\{F[k]\}\}$ is the periodic convolution kernel to produce $\mathrm{Im}\{\tilde{x}[n]\}$. $\mathrm{Od}\{F[k]\}$ (e.g., [0 1 1 1 0 −1 −1 −1]) is the longest bipolar pulse as an odd discrete finite-length sequence. Therefore, the time localization of $F[k]$ (e.g., $\mathrm{DFT}^{-1}\{[0\ 1\ 1\ 1\ 0\ -1\ -1\ -1]\}$) is not wider than that of any $F'[k]$. Consequently, the instantaneous phase associated with $F[k]$ is well time-localized.

Because of the aforementioned characteristics, $F[k]$ is sufficient for phase-interpolated averaging. Although some $F'[k]$ may work as well as $F[k]$, there is no good way to find such an $F'[k]$ among such huge variations.

REFERENCES

[1] S. Makeig, M. Westerfield, T. P. Jung, S. Enghoff, J. Townsend, E. Courchesne, and T. J. Sejnowski, "Dynamic brain sources of visual evoked responses," *Science*, vol. 295, pp. 690–694, 2002.

[2] Y. Naruse, A. Matani, T. Hayakawa, and N. Fujimaki, "Influence of seamlessness between pre- and post stimulus alpha rhythms on visual evoked potential," *NeuroImage*, vol. 32, pp. 1221–1225, 2006.

[3] C. Tallon-Baudry and O. Bertrand, "Oscillatory gamma activity in humans and its role in object representation," *Trends Cogn. Sci.*, vol. 3, pp. 151–162, 1999.

[4] E. Rodriguez, N. George, J. P. Lachaux, B. Renault, and F. J. Varela, "Perception's shadow: Long-distance synchronization of human brain activity," *Nature*, vol. 397, pp. 430–433, 1999.

[5] A. Matani, Y. Naruse, Y. Terazono, T. Iwasaki, N. Fujimaki, and T. Murata, "Phase-compensated averaging for analyzing electroencephalography and magnetoencephalography Epochs," *IEEE Trans. Biomed. Eng.*, vol. 57, no. 5, pp. 1117–1123, May 2010.

[6] P. Sauseng, W. Klimesch, W. R. Gruber, S. Hanslmayr, R. Freunberger, and M. Doppelmayr, "Are event-related potential components generated by phase resetting of brain oscillations? A critical discussion," *Neuroscience*, vol. 146, pp. 1435–1444, 2007.

[7] B. K. Min, N. A. Busch, S. Debener, C. Kranczioch, S. Hanslmayr, A. K. Engel, and C. H. Herrmann, "The best of both worlds: phase-reset of human EEG alpha activity and additive power contribute to ERP generation," *Intl. J. Psychophysiol.*, vol. 65, pp. 58–68, 2007.

[8] V. V. Nikulin, K. Linkenkaer-Hansen, G. Nolte, S. Lemm, K. R. Müller, R. J. Ilmoniemi, and G. Curio, "A novel mechanism for evoked responses in the human brain," *Eur. J. of Neurosci.*, vol. 25, pp. 3146–3154, 2007.

[9] E. Niedermeyer and F. L. da Silva, *Electroencephalography*, 5th ed. Baltimore, MD: Lippincott Williams and Wilkens, 2005.

[10] A. V. Oppenheim and R. W. Schafer, *Discrete-time Signal Processing*, 2nd ed. Upper Saddle River, NJ: Prentice Hall, 1999.

[11] A. Mazaheri and O. Jensen, "Posterior α activity is not phase-reset by visual stimuli," *Proc. Natl. Acad. Sci. USA*, vol. 103, pp. 2948–2952, 2006.

[12] B. Boashash, "Estimating and interpreting the instantaneous frequency of a signal—Part 1: Fundamentals," *Proc. IEEE*, vol. 80, no. 4, pp. 520–538, Apr. 1992.

Ayumu Matani (M'96) received the B.E., M.E., and Ph.D. degrees in control engineering from Osaka University, Osaka, Japan, in 1989, 1991, and 1998, respectively.

From 1991 to 1995, he was with Osaka Gas Company Ltd. From 1995 to 1998, he was with Nara Institute of Science and Technology. He is currently an Associate Professor at Graduate School of Frontier Sciences, the University of Tokyo, Kashiwa, Japan, and an Invited Researcher at Biological Information and Communication Technology (ICT) Group, National Institute of Information and Communication Technology, Kobe, Japan. His research interests include signal processing, complex system theory, and brain imaging.

Yasushi Naruse received the B.E. degree in mathematical engineering and information physics from the University of Tokyo, Tokyo, Japan, and the M.S. and Ph.D. degrees in complexity science and engineering from the University of Tokyo, Kashiwa, Japan, in 2002, 2004, and 2007, respectively.

He is currently a Researcher at the Biological ICT Group, National Institute of Information and Communication Technology, Kobe, Japan. His research interests include signal processing and modeling of neural activities.

Yasushi Terazono received the B.E. and M.E. degrees in mathematical engineering and information physics, and the Ph.D. degree in complexity science and engineering from the University of Tokyo, Tokyo, Japan, in 1999, 2001, and 2004, respectively.

From 2004 to 2009, he was with the National Institute of Information and Communication Technology, Kobe, Japan. He is currently a Postdoctoral Fellow at Graduate School of Frontier Sciences, the University of Tokyo, Kashiwa, Japan. His research interests include inverse problems and mathematical programming.

Norio Fujimaki (M'80) received the B.E., M.E., and Ph.D. degrees in electronics engineering from the University of Tokyo, Tokyo, Japan, in 1975, 1977, and 1980, respectively.

From 1980 to 1999, he was with Fujitsu Laboratories Ltd., Atsugi, Japan. Since 1999, he has been a Senior Researcher at Biological ICT Group, National Institute of Information and Communication Technology, Kobe, Japan. He has also been a Visiting Professor at Graduate School of Life Science and Systems Engineering, Kyushu Institute of Technology, Kitakyushu, Japan, since 2001, and at Human Information System Laboratories, Kanazawa Institute of Technology, Kanazawa, Ishikawa, Japan, since 2005. His research interest includes measurements of linguistic brain functions.

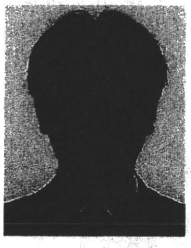

Tsutomu Murata received the B.S., M.S., and Ph.D. degrees in pharmaceutical sciences (biophysics of the brain) from the University of Tokyo, Tokyo, Japan, in 1985, 1987, and 1993, respectively.

From 1992 to 1998, he was with Kanazawa Institute of Technology, Kanazawa, Ishikawa, Japan. He is currently the Subleader of Biological ICT Group, National Institute of Information and Communication Technology, Kobe, Japan. His research interests include psychophysics and neuroscience of emergent visual recognition.

感覚神経線維刺激を用いた義手への感覚提示機能の実装に関する研究

Study for a mounting technique for experiencing sensory sensation to prosthetic hand by electrical stimulating sensory nerve fiber

○新納 弘崇 (電通大)　荒木 望 (兵庫県立大)　國本 雅也 (済生会横浜市東部病院)　帆足 勇希 (兵庫県立大)
鈴木 隆文 (東京大)　深山 理 (東京大)　満渕 邦彦 (東京大)　下条 誠 (電通大)

H.Niiro(UEC),N.Araki(Univ. of Hyogo),M.Kunimoto(Saiseikai Hosp.),Y.Hoashi(Univ. of Hyogo)
T.Suzuki(Univ. of Tokyo),O.Fukayama(Univ. of Tokyo),K.Mabuchi(Univ. of Tokyo),M.Shimojo(UEC)

Abstract— This paper presents a mounting technique for experiencing sensory sensation to prosthetic hand with which patients lost the extremities by disturbances will be able to replace the extremities and feel somatic sensation as if they were touching an object with their healthy hand. The system consists of myoelectric prosthetic hand by surface electromyography signal and flexible pressure sensors which cover the finger of prosthetic hand and micro-electrical stimulation of the sensory nerve fibers was used in order to evoke somatic sensations. The results show that the system worked satisfactorily, and it is demonstrated that the system will be able to compensate sensory function of the patients with sensory neuropathy and have possibilities for replace the extremities

Key Words: sensory feedback,prosthetic hand,work support,microstimulation method

1. 緒言

事故等による障害によって上肢を失ってしまい，日常生活に復帰するには義手の装着を余儀なくされる．しかし，一般的な義手は装着者の運動を代替するものではなく，また感覚機能を備えることはない．そこで，障害によって失った上肢に代替する一つの方法として，筋電位を使用した義手が研究され [1]，感覚機能を補う一つの方法として，感覚神経を機能的電気刺激 (Functional Electrical Stimulation(FES)) によって刺激することで感覚提示する研究がなされるようになった [2]．そこで，我々は失った腕を代替する方法として上記の技術を応用し，表面筋電位により義手操作を行い，マイクロスティミュレーション法により感覚提示を行い，失った腕を代替するシステムの構築を行った．本稿では，構築したシステム，実験結果について報告する．

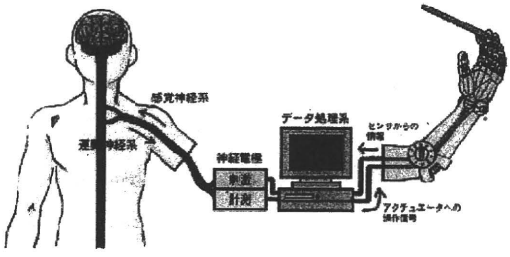

Fig.1 The concept of the proposed system.

2. 実験システム

実験システムの全体構成を図 2 と図 3 に示す．システムは筋電義手と感覚提示の 2 つから構成される．図 2 の筋電義手は，表面筋電信号から義手の関節角度を推定し，義手を駆動する．図 3 の感覚提示は，筋電義手に実装した圧力センサ (FingerTPS) の信号を神経刺激信号用 PC に取り込み，信号に応じて神経線維を刺激するパルス列を出力する．以下各実験システムについて説明する．

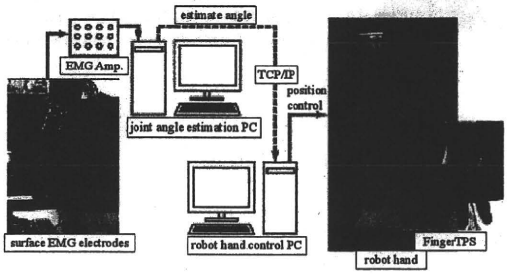

Fig.2 The experimental arrangement side of prosthetic hand.

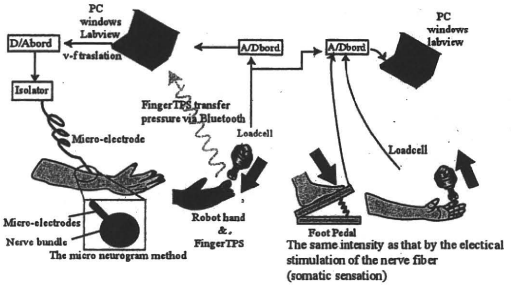

Fig.3 The experimental arrangement side of experiencing sensory sensation.

2.1 義手

義手として川渕機械技術研究所の特注仕様のロボットハンドを用いた．手指部分で 15 自由度をもち，DC モータにより駆動する．義手の操作法は [1] にて報告された手法を用いた．

2.2 圧力 (感覚) センサ

義手に装着した圧力センサは FingerTPS(PPS 社製) を用いた．圧力センサは接触力を検出するフレキシブルな静電容量型圧力センサである．出力は Bluetooth 通信で PC に接続され，更新周波数は 40Hz である．

2.3 神経線維インターフェース

感覚センサからの情報を基にマイクロスティミュレーション法を用いて感覚を被験者に提示する．マイクロスティミュレーション法とは，経皮的に微小針電極を腕の正中感覚神経線維の中に刺入し，電気刺激パルス列を入力することで，人工感覚を生成する手法である．

Fig.4 Prosthetic hand & FingerTPS

Fig.5 The manner in which microstimulation is performed.

3. 義手の感覚フィードバック実験

電気刺激頻度と感覚強度の関係の例を図6に示す．図6のように，感覚神経への電気刺激によって生成される圧感覚の強度は，パルス頻度に依存している事が報告 [3] されており，本研究ではこの関係を応用する．

実験の様子を図7に示す．被験者は健全な男性1名，座位・開眼状態で実験を行った．義手に加えた力により発生する感覚と等価な感覚量を感覚神経の電気刺激で発生させることを目的とする．

まず，義手の運動制御用の表面筋電電極を測定対象とする筋上の皮膚の2か所接近させて貼りつけ，その差動電位として筋電信号の電位活動の計測と記録を行なった．なお，接地電極の装着は左手肘外側部に行なった．その後，微小針電極を刺入し，義手の圧力センサを加圧し，実験を行った．本稿では，生成された感覚強度の評価法として，加圧した義手に発生した力と反対の指先でその力に対し等価な感覚量を提示させる方法と，足元に設置したペダルを踏み込む方法の2つとした．義手の指先にFingerTPSを装着し，FingerTPSの出力をパルス列頻度に変換・出力し，マイクロスティミュレーション法によりパルス列を神経に伝達することで感覚を提示した．

本実験での圧覚から電気刺激のパルス列頻度への変換式は，FingerTPSの出力 x を係数 a にて整数倍し，パルス頻度の周波数 f とした．即ち，$f = ax$ で，本実験では $a = 10$ とした．この変換係数を変更することで被験者に発生する感覚強度の感度を変更できる [2]．

実験結果を図8に示す．グラフは上からFingerTPSと加圧力，指先による感覚量とペダルによる感覚量，刺激パルス列周波数，刺激パルス列である．実験結果をみると，FingerTPSが検出する圧力の増加に追従するように，若干の時間差をもって被験者の感覚量が増加していることがわかる．指先による感覚量とペダルによる感覚量の変化に大きな違いはみられず，被験者の感覚強度を忠実に表現していることがわかる．

4. 結言

義手に装着した感覚センサの出力をマイクロスティミュレーション法により感覚神経フィードバックし，人工感覚を提示するシステムを構築し，義手に加わった圧力を感覚として被験者に提示する実験に成功した．今後，義手を筋電により操作し，アクティブに加わる圧力を感覚神経フィードバックする．

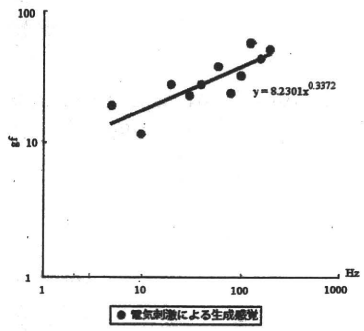

Fig.6 Relationship between pushing force and somatic sensations

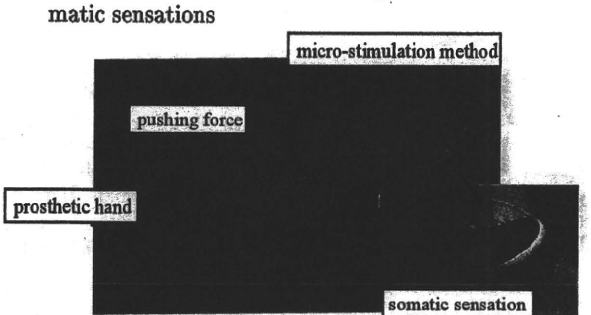

Fig.7 Quantitative evaluation of the pressure sensation evoked by microelectrical stimulation.

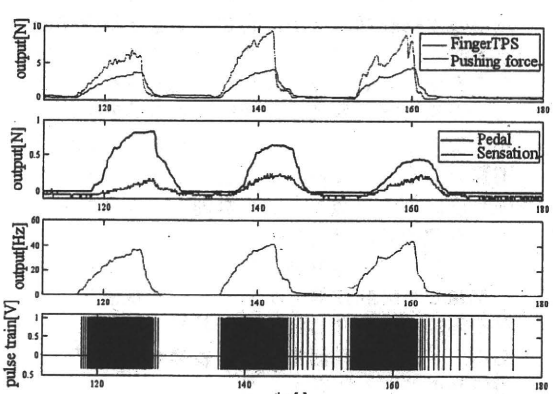

Fig.8 Response of subjective pressure sensation evoked by the microelectrical stimulation, pulse train for the microelectrical stimulation, and the actual force applied to the Finger TPS system,

文 献

[1] 荒木望, 帆足勇希, 小西康夫, 満渕邦彦, 石垣博行"表面筋電信号ヒストグラムによる複数指関節角度推定-ベイジアンフィルタによる動作指識別を用いた手法-",BPES,2010

[2] 新納弘崇, 國本雅也, 鈴木隆文, 満渕邦彦, 下条誠"感覚神経系患者のためのフェアラブル感覚補填・感覚強化システムの開発-マイクロスティミュレーション法による触圧覚生成と感覚増強-",Robomech,2010

[3] T.Suzuki,K.Mabuchi,H.Nishimura,T.Saito,N.Kakuta, M.Kunimoto,M.Shimojo,"The Relationship between Stimulation Signals and Subjective Intensities and Areas", Proc. Int. Conf. of the IEEE EMBS,Atlanta, 459, Oct. 1999.

義手の運動制御のための生体信号からの手指関節角度推定
—表面筋電信号と針筋電信号を中心とした信号源の違いによる処理方法の検討—

Finger Joint Angle Estimation Using Biosignal For a Mioelectric Hand Motion Control
-A Study of Signal Processing Method for Surface EMG Signal and Needle EMG Signal-

○正　荒木　望（兵庫県立大）　非　帆足　勇希（兵庫県立大）　正　小西　康夫（兵庫県立大）
正　満渕　邦彦（東京大学）　正　石垣　博行（兵庫県立大）

Nozomu ARAKI, University of Hyogo, araki@eng.u-hyogo.ac.jp
Yuki HOASHI, University of Hyogo
Yasuo KONISHI, University of Hyogo
Kunihiko MABUCHI, University of Tokyo
Hiroyuki ISHIGAKI, University of Hyogo

This study aims to control a mioelectric hand motion using neural signal. Consequently, we consider to establish a method estimated finger joint angle from biosignal. We have previously proposed a finger joint angle estimation method based on surface Electromyography (EMG) signal and a linear model. This method is based on the histogram of signals, it may have applicability to not only surface EMG signals but also neural signals. Therefore, this paper carried out finger joint angle estimation experiment using both surface EMG signals and needle EMG signals that are similar to neural signals. Here, we report on the difference of estimation results using both signals.

Key Words: Biosignal, Electromyography (EMG) Signal, Joint Angle Estimation

1. 緒言

近年，事故や疾病により手を失った患者のために，失われた手の運動機能を補う能動義手の研究が盛んに行われている．義手の運動制御のために必要となる手指や関節角度を推定する手法については，その多くが皮膚表面で非侵襲的に計測しうる表面筋電信号を対象として提案されている．しかしながら，表面筋電信号は電極周辺にある筋群の活動を統合的に計測した信号であり，また深部の筋肉の活動情報を得ることが困難であることから，対象とする筋肉のみの活動を抽出・評価するためには種々の信号処理手法を必要とする．これに対して筋電信号にはもう一つ，測定対象の筋肉内に針電極を刺入することで，運動神経活動に伴った筋線維の収縮活動を直接記録した針筋電信号がある．針筋電信号には，測定対象となる筋肉の純粋な活動情報を計測できるという大きな長所がある．一方で，針筋電信号は侵襲的手法であり，安定した筋電信号の計測が困難であることから，現在のところ義手制御には用いられていない．

義手の動きを制御する際に用いうる可能性のあるもう一つの生体情報に，上記の筋肉の収縮を指令する運動神経信号がある．筋電信号を用いる場合には測定対象となる筋が残存している必要があり，すべての上肢切断者に適用できるわけではない．これに対して神経信号は，対象となる筋肉が失われていても筋肉の収縮を指令する信号を出力していると考えられる．このため我々は神経信号を用いた義手の運動制御を最終目標としている．しかしながら，神経信号の測定は容易ではなく，また，処理手法も未だ確立されていないため，現在はその代替信号として筋電信号を用いた手指関節角度推定法の検討を行っており，このなかで，測定した表面筋電信号のピーク値の分布であるヒストグラムを算出し，得られたヒストグラムと指関節角度の関係を線形モデルとして推定する手法を既に提案している[1, 2, 3]．この手法は，針電極によって測定した針筋電信号を用いた関節角度推定手法[4, 5]を表面筋電信号に応用したものであり，表面筋電信号を針筋電信号と同様のパルス信号の集合とみなしてデジタル的に処理する手法である．このため本手法はアルゴリズムを変更することなく，針筋電信号や本研究の最終目標である神経信号へ適用できる可能性がある．以上の背景から本稿では，同時測定を行った表面筋電信号と針筋電信号から，各信号が有する情報の差異を検証すると共に，我々の提案した角度推定手法が針筋電信号に対しても適用可能であるかどうかの検証を試みた．

2. 筋電信号測定条件

はじめに，本稿で使用した筋電信号の測定条件について述べる．本稿における実験では被験者の左手第 3 指の MP 関節および PIP 関節についての推定を行うため，図 1 に示すように表面筋電信号および針筋電信号はともに第 2，3 指の動作に動員される浅指屈筋および総指伸筋の 2 箇所で測定するものとした．このうち，表面筋電信号測定用の電極は，ディスポ電極（日本光電製 M-150）の電極部（直径 10mm）のみを 2 個 1 組として使用するものとし，測定時には電極間距離が中心間距離で 20mm となるように貼り付けた．また，針筋電信号測定用の電極は直径 125μm のマイクロニューログラム用針電極を使用するものとした．これらの筋電位の計測には日本光電製生体アンプを使用し，表面筋電信号についてはゲインを 0.1mV/V，測定周波数帯域を 15～1kHz とし，針筋電信号についてはゲインを 50μV/V，測定周波数帯域を 150～10kHz と設定した．なお，これらの信号のサンプリングは 2500Hz で行うものとした．さらに今回の実験では，被験者の手指の角度に

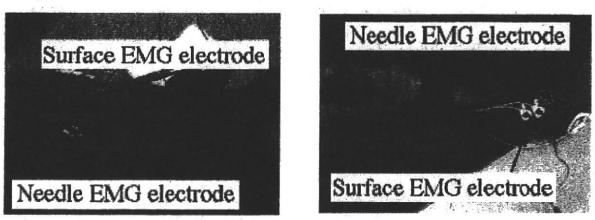

(a) Flexor muscle side　(b) Extensor muscle side

Fig.1 Electrode positions for surface and needle EMG signal.

ついてはデータグローブ（CyberGlove）を使用し，指を伸展した状態を0度として各関節の屈曲角度を測定するものとした．

3. 表面筋電信号および針筋電信号の同時測定結果

本実験では前章で述べた測定条件で，表面筋電信号，針筋電信号，および左手第3指のMP，PIP関節角度の同時測定を行った．実際に測定した筋電信号の一例を図 2 に示す．図 2 中・下段に示す針筋電信号および表面筋電信号はそれぞれ図1(b)に示した総指伸筋の筋腹付近で，第 3 指の屈曲・伸展動作を繰り返し行った際の信号を測定したものである．これらの信号は振幅の大きさが異なるものの，互いに似通ったパルス（スパイク）状の波形をもつことが分かる．図 2 中段に示す針筋電信号を見ると，指を伸展させた際にパルス状の波形が現れており，屈曲時にはパルス状の波形を全く出力していないことが分かる．一方，図2下段の表面筋電信号では，屈曲・伸展どちらの場合にもパルス状の波形が現れており，伸展時により大きな振幅の波形が現れていることが分かる．これは，総指伸筋の深層部の信号を測定している針筋電信号では，伸筋の動作時のみにパルス状の波形が現れるが，表面筋電信号は皮膚表面から深層部の筋の信号が減衰・積分された信号を捉えているために，伸筋の信号だけでなく周囲の屈筋で発生した信号が重畳しているためであると考えられる．

本稿では，図 2 のように同時測定した表面筋電および針筋電信号を用いて指関節角度推定を試みた．次章では，本稿で使用する指関節角度推定手法について簡単に述べる．

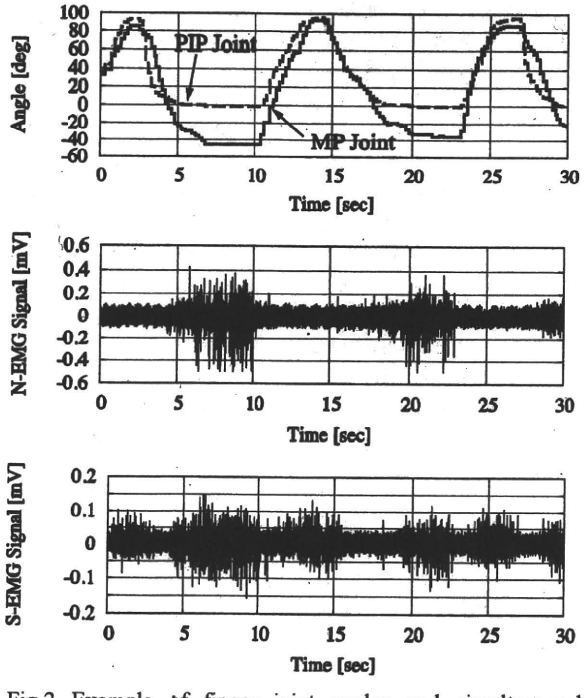

Fig.2 Example of finger joint angles and simultaneously measured EMG signals. (top: MP joint and PIP joint angles which measured by data glove, middle: needle EMG signal, bottom: surface EMG signal)

4. 筋電信号ヒストグラムによる関節角度推定法

ここでは文献[1, 2, 3]において著者らが提案した表面筋電信号のヒストグラムを用いた指関節角度推定法について述べる．本手法の特徴は，表面筋電信号の振幅や周波数特性といったアナログ情報を使用せずに，筋が活動した際に表面筋電信号

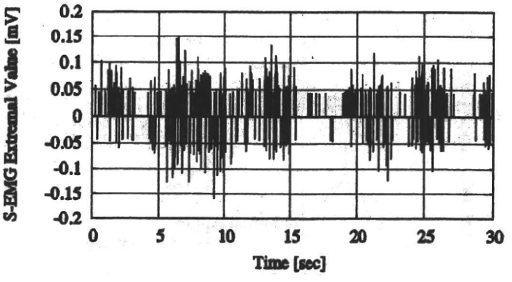

Fig.3 Extremal value of surface EMG signal shown in figure 2.

に現れるパルス状の波形の頻度とピーク値の大きさに着目する点である．

本手法では角度推定を行うために，図 2 下段のような表面筋電信号からピーク値のヒストグラムを算出する．ヒストグラムを算出する際には，取得した筋電信号に定常的に存在するノイズを閾値処理により消去し，残ったパルス状の信号のピーク値（極値）のみを取り出す処理を行う．図 3 は，図 2 下段の表面筋電信号から極値のみを取り出した信号である．本手法では図 3 に示すような極値のみの信号からヒストグラムを得るために，信号の振幅の絶対値によって信号強度を 6 つの領域に分割し，0.5 秒分の取得データからそれぞれの領域での頻度 $X_1,\ldots,X_6$ を算出するものとした．

いま，時刻 t において屈筋側の筋電信号から求めたヒストグラムを $\{X_1^f(t),\ldots,X_6^f(t)\}$，伸筋側から求めたヒストグラムを $\{X_1^e(t),\ldots,X_6^e(t)\}$ とする．指関節角度は屈筋と伸筋のバランスにより決定されると考えられるため，ある指の関節角度 $\theta(t)$ はこれらのヒストグラムから以下の式により与えられると仮定する．

$$\hat{\theta}(t) = \theta_0 + \sum_i^6 \left\{ a_i X_i^f(t) + b_i X_i^e(t) \right\} \qquad (1)$$

ここで a_i，b_i は屈筋および伸筋側の筋電信号ヒストグラムに対する重み係数であり，θ_0 はバイアス成分である．これらのパラメータについては，学習用にデータグローブで測定した指関節角度と，同時に計測した筋電信号から計算されたヒストグラムを用いて最小二乗法により得られる．したがって，本手法における指関節角度の推定値 $\hat{\theta}(t)$ は，測定した筋電信号のヒストグラムから式(1)を用いて計算される．

以上が本稿で用いる指関節角度推定手法である．この手法については，リアルタイムで関節角度を推定する実験を行い，表面筋電信号を用いた場合については有効性を既に確認している[2, 3]．また，上記のアルゴリズムからも分かるように，本手法は信号のピーク値(極値)の振幅と頻度のみを特徴量として扱っている．これは，先行研究である文献[4, 5]において，針筋電信号のパルス波形の発火頻度が筋張力と線形の相関をもつことが示されていることに起因している．このため本手法による指関節角度推定は，表面筋電信号だけではなく，針筋電信号や神経信号といった異なる信号源に対してもアルゴリズムを変更することなく適用できる可能性がある．そこで本稿では，第 3 章で述べた表面筋電および針筋電信号の同時測定結果に本手法を適用し，異なる信号源からの筋電信号を用いた指関節角度推定実験を行うこととした．

5. 指関節角度推定実験

ここでは前章で述べた我々の提案法による，表面筋電と針筋電信号からの指関節角度推定実験について述べる．実験では，第 2 章で述べた測定条件で被験者の表面筋電信号，針筋電信号および手指の関節角度の計測を行った．また今回は，

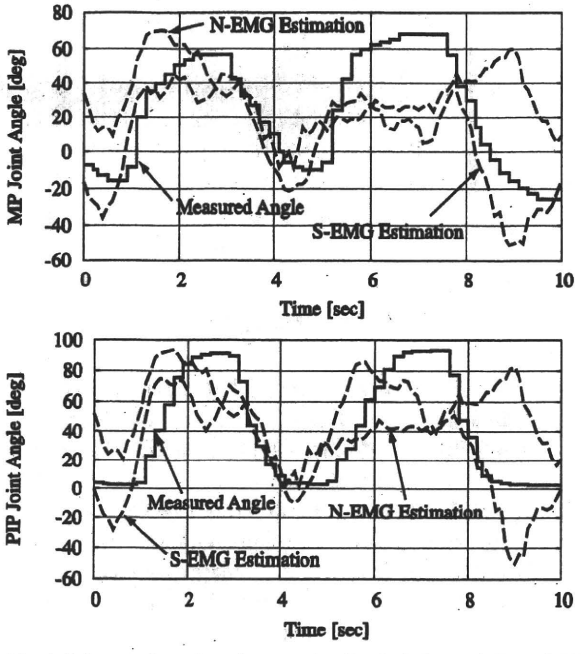

Fig.4 Joint angle estimation results for 3rd finger MP and PIP joint and its measured values. (top: MP joint angle results, bottom: PIP joint angle result, solid-line: measured angle, dashed-line: estimation result using surface EMG signals, dotted-line: estimation result using needle EMG signals.)

これらの計測信号と第 4 章で述べた角度推定法を実装した筋電義手シミュレータを用いて，第 3 指の MP，PIP 関節角度をリアルタイムで推定することとした．本実験では，被験者の左手第 3 指の屈曲・伸展動作を連続的に 60 秒間繰り返した際の表面筋電信号および針筋電信号を計測し，この計測結果から(1)のパラメータ a_i，b_i および θ_0 を最小二乗法で計算した．次に，得られたパラメータと計測した筋電信号からリアルタイムで角度推定を行い，表面筋電信号と針筋電信号による推定結果の違いについて検証を行った．

図 4 に表面筋電信号および針筋電信号から推定した第 3 指の MP 関節角度および PIP 関節角度と，データグローブにより測定した実際の角度との比較結果を示す．図 4 から，表面筋電信号および針筋電信号どちらの推定結果も実測値から誤差があるものの，実測結果に追従する傾向を示していることが判る．なお，表面筋電信号については，今回の実験では表面筋電と針筋電を極力同じ位置で測定することを主眼においており，通常，表面筋電信号が良好に測定できる位置とは異なる場所に電極を貼り付けたために推定精度が悪化したものと考えられる．また，針筋電信号による推定結果については，今回の実験では屈筋側の信号が良好に計測できていなかったことが指の屈曲時の推定精度を悪化させる一因になっていると考えられる．しかしながら，図 4 の 3〜4 秒付近のように，表面筋電信号および針筋電信号のどちらの推定結果も実測結果によく追従している部分も見受けられる．以上の結果より，推定精度に関しては問題が残るものの，我々の提案手法を用いることで，アルゴリズムを変更することなしに表面筋電信号および針筋電信号のどちらからでも指関節角度の推定が行える可能性を示唆した．

6. 考察

今回の表面筋電信号と針筋電信号の同時測定，および，これらの信号を用いて同一アルゴリズムで指の角度推定実験を行った結果，以下のような点が明らかとなった．

- 同一部位で表面筋電信号および針筋電信号を同時に計測した結果，針筋電信号では電極を刺入した筋に関連する信号のみが観測されたが，表面筋電信号では周囲の筋の情報も重畳した信号が観測された．
- 筋電信号のヒストグラムと線形モデルを使用することにより，表面筋電信号および針筋電信号のどちらを用いても指関節角度推定が行える可能性が示された．

一方，今回の実験から，信号測定方法およびアルゴリズムについていくつかの問題点が明らかとなった．まず，信号測定方法については以下のような問題点を確認した．

- 針筋電信号を用いて角度推定を行う場合，今回用いた針電極を経皮的に筋肉に刺入する方法では，筋の動作により刺入された電極位置が変化し，信号の形状が変化する．
- 表面筋電と針筋電を比較すると表面筋電信号の方が安定した計測が容易であり，針筋電信号の方が周囲のノイズの影響を受け易い．

これらの問題については，針筋電の電極の固定方法，および，ノイズ対策について検討を行う必要がある．また，角度推定アルゴリズムに関しては，ヒストグラムを作成するための信号強度の分割数，および，分割領域について，針筋電に対しての最適値を検討する必要がある．なお，指の屈曲を保持した際に，角度の推定結果が振動的になるという問題については表面筋電信号を用いた実験でも確認していたが，針筋電信号を使用した場合にはより顕著になる事も確認した．特に推定結果の振動の問題については，実際に義手を動かす際には大きな問題となるので，この振動を抑制することが本研究の今後の重要な課題である．

7. 結言

本稿では，義手制御のための生体信号からの手指関節角度推定手法の確立を目的として，表面筋電信号と針筋電信号の同時測定を行い，各信号が有する情報の差異を明らかにした．また，既に提案した角度推定手法が針筋電信号に対しても適用可能であるかどうかの検証を行うため，同一部位で計測した表面筋電信号と針筋電信号を用いて被験者の第 3 指 MP 関節および PIP 関節の角度推定実験を行った．実験の結果，我々の提案手法を用いることで，アルゴリズムを変更することなしに表面筋電信号および針筋電信号のどちらからでも指関節角度の推定が行える可能性を示唆した．

文 献

[1] 山水康隆, 荒木望, 小西康夫, 満渕邦彦, 石垣博行, “表面筋電信号のヒストグラムを用いた指関節角度推定法”, 第 23 回生体・生理工学シンポジウム, pp.183-184, 2008.

[2] Y. Hoashi, Y. Yamamizu, N. Araki, Y. Konishi, K. Mabuchi and H. Ishigaki, “Estimation of Finger Joint Angle Based on Surface EMG Signals and its Signal Source Recognition”, ICIC Express Letters, Vol.4, No.6(A), pp.2183-2188, 2010.

[3] 荒木望, 帆足勇希, 小西康夫, 満渕邦彦, 石垣博行, “表面筋電信号ヒストグラムによる複数指関節角度推定 –ベイジアンフィルタによる動作指識別を用いた手法-”, 第 25 回生体・生理工学シンポジウム, pp.151-154, 2010.

[4] 古川浩太郎, 鈴木隆文, 満渕邦彦, “末梢運動神経信号による義手制御のための基礎的研究 –針筋電信号による握力及び関節角度の推定-”, 第 36 回日本臨床神経生理学会予稿集, pp.413-414, 2006.

[5] 高橋玄顕, 満渕邦彦, 鈴木隆文, “針筋電信号を用いた指の運動の推定 –神経回路モデルの有効性と適用方法の検討-”, 生体医工学, 第 46 巻 CD-ROM, 2008.

Development of a Wearable Sensory Prosthetic Device for Patients with Peripheral Neural Disturbances

Mabuchi K[1], Niiro H[2], Kunimoto M[3], Suzuki T[1], Ishikawa M[1], Shimojo M[2]

[1] Graduate school of Information Science and Technology, The University of Tokyo, Tokyo, Japan

[2] Faculty of Electro-communications, The University of Electro-communications, Chofu, Japan

[3] Saiseikai Yokohamashi Tobu Hospital, Yokohama, Japan

Abstract

This paper presents a prototype of a wearable sensory prosthetic system with which patients suffering from peripheral sensory disturbances and lost sensory function of the extremities will be able to feel somatic sensations as if they were touching an object with their healthy hand. Test results indicate that the system will be able to compensate or even enhance the sensory function that has been lost due to peripheral neuropathy.

The system consists of flexible fingerstalls and a palm patch equipped with pressure sensors and percutaneous micro-electrical stimulation to sensory nerve fibers of the peripheral nerve was used in order to evoke pressure sensation to the subject.

The results show that the system works satisfactorily, with subjects able to feel the pressure sensation resulting from the pressure applied to the pressure sensor of the fingerstall.

There was also a good correlation between the pressure applied to the pressure sensor system and the subjective intensities of the evoked pressure sensations.

***Keywords**: sensory prosthetics, microstimulation, artificial somatic sensation*

Introduction

For people whose peripheral nerve functions have been lost or disturbed due to injury or diseases, it is very important to substitute for their lost neural functions in some way.

Functional electrical stimulation (FES) has been widely studied as a way to substitute for motor functions, but it has not been thoroughly examined for the substitution of sensory functions.

In this study, we developed a prototype of a sensory prosthetic system for patients who have lost the sensory function of the extremities due to peripheral nerve injury or peripheral neuropathy.

The system is composed of a fingerstalls and a palm patch equipped with pressure sensors. The sensors detect mechanical stimuli, which are transferred stimuli to the subject by means of a microstimulation method so that the subject experiences the stimuli as the corresponding somatic sensations [1].

In trials, the system worked satisfactorily and there was a good correlation between the pressure applied to the pressure sensors and the subjective intensities of the evoked pressure sensations.

Material and Methods

One healthy male subject participated in the experiment. Experimental arrangement is shown in Fig.1. The system consists of the two subsystems, one for sensing mechanical stimuli and the other for stimulating sensory nerve fiber.

Microstimulation Method

The microneurographic technique involves the percutaneous and direct insertion of a tungsten microelectrode into a peripheral nerve so that the signal from the nerve fiber attached to the tip of the electrode can be measured and so that a microstimulation can be given to the nerve fiber.

There are mainly four kinds of mechanosensitive receptors on the skin: Merkel discs, Ruffini endings, Meissner corpuscles, and Vater-Pacini corpuscles [2]. The response of these receptors is classified into four patterns: slowly adapting I (Merkel), slowly adapting II (Ruffini), rapidly adapting type (RA: Meissner), and Pacinian type (PA: Vater-Pacini).

Ochoa et al have reported that a pressure sensation is evoked by stimulating an SA-I mechanoreceptor unit and that the magnitude of the evoked sensation is influenced by the